

# **1 Downwind control of oceanic air by land: the land**

## **2 wake and its sensitivity to CO<sub>2</sub>**

**3 Marysa M. Laguë<sup>1,2\*</sup>, Gregory R. Quetin<sup>3</sup>, and William R. Boos<sup>2,4</sup>**

**4** <sup>1</sup>Coldwater Lab, Center for Hydrology, University of Saskatchewan, Canmore, AB, Canada

**5** <sup>2</sup>Department of Earth and Planetary Science, University of California, Berkeley, Berkeley, CA, USA

**6** <sup>3</sup>Department of Geography, University of California, Santa Barbara, CA 93016, USA

**7** <sup>4</sup>Climate and Ecosystem Sciences Division, Lawrence Berkeley National Laboratory, Berkeley, CA, USA

**8** \*marysa.lague@usask.ca

### **9 ABSTRACT**

Oceans are well-known to be directly altered by global climate forcings such as greenhouse gas changes, but how oceans are indirectly influenced by land and its response to such forcings remains less explored. Here, we assess the present-day and projected future state of a little-explored feature of the climate system – a “land wake” in relative humidity downwind of the east coast of North America, consisting of low-humidity continental air extending roughly 1,000 km over the Atlantic ocean. The wake exists throughout the year, but is supported by high continental temperatures in summer and low continental moisture in winter. The wake is well represented in an ensemble of global climate models (GCMs), qualitatively matching reanalysis data. Under increasing atmospheric CO<sub>2</sub>, the land wake intensifies in GCM simulations through two pathways: the radiative effects of CO<sub>2</sub> on surface temperatures, and the biogeochemical effect of CO<sub>2</sub> on terrestrial vegetation. Vegetation responses to increased CO<sub>2</sub> alter the summer wake from Florida to Newfoundland, and both the radiative and biogeochemical effects of CO<sub>2</sub> drive reductions in coastal cloud cover. These changes illustrate the potential of rapidly changing terrestrial climate to influence coastal regions and the ocean environment downwind of continents through both light conditions and the energy balance of the surface ocean.

### **11 1 Introduction**

Differences in the surface properties of ocean and land produce large asymmetries in the interaction of these two components of the climate system with the overlying atmosphere. Oceans have a large heat capacity and slow dynamics ([Cess and Goldenberg, 1981; North et al., 1983](#)), which allow years-long variations in sea surface temperature to drive atmospheric circulations that influence climate in remote continental regions ([Myneni et al., 1966; Perry et al., 2017; Yang and Delsole, 2012](#)). Land lacks sufficient heat capacity to create such persistent thermal forcings, but continents alter the atmosphere mechanically, e.g. by generating orographic stationary waves that dominate the northern hemisphere circulation in winter ([Cook and Held, 1992; Held et al., 2002; Maroon et al., 2015; White et al., 2017](#)), and by generating seasonal thermal forcings such as those that drive

19 cross-equatorial monsoon circulations (Boos and Kuang, 2013; Li and Yanai, 1996; Wu et al., 2012). In this study, we quantify  
20 and explore the mechanisms governing a little-explored feature of the climate system – a “land wake” consisting of maritime  
21 air that has been perturbed by the passage of prevailing winds over a continent.

22 We are motivated by the fact that land and ocean influence each other by serving as sources for tracers that are carried by  
23 winds. Oceans serve as the primary source of moisture and of pristine, unpolluted air for continents (Parrish and Hahn, 1992;  
24 Robertson et al., 2016). Past studies have examined how continental air masses that are transported over ocean transform the  
25 aerosol content of the marine boundary layer (Fu et al., 2018; Fuchs et al., 2017), influencing cloud properties over ocean  
26 (Fuchs et al., 2017; Garrett and Hobbs, 1995). Seasonal differences in high-latitude cold air outbreaks impact the seasonality  
27 of aerosol nucleation (Nilsson et al., 2001). Outbreaks of dry and dusty air from the Sahara have been shown to episodically  
28 alter the thermal structure and likelihood of tropical cyclogenesis over the Atlantic (Carlson and Prospero, 1972). As polar  
29 continental air transitions to polar maritime air, its moisture content increases due to ocean evaporation, altering both the  
30 temperature and moisture content of the air mass (Burke, 1945). Movement of air masses between continental and maritime  
31 regions is responsible for numerous weather phenomenon including cold air outbreaks and high-latitude cyclogenesis (Businger  
32 and Reed, 1989; Pithan et al., 2018). The larger diurnal temperature cycle of land drives land-sea breezes (Gannon, 1978; Gille  
33 et al., 2005; Sonu et al., 1973).

34 The fact that source regions, such as continents, can imprint themselves on the thermodynamic state of air motivated  
35 Bergeron’s widely used air mass classification system (?) and its modifications, e.g. for the Americas (?). Such systems  
36 generally classify air as being either continental or maritime in origin, and also polar or tropical in origin, motivated by  
37 the recognition that transient extratropical cyclones mix air meridionally (?). Such classification was often qualitative and  
38 subjective, but numerical objective approaches have been used (??) and secular trends in air mass characteristics have been  
39 analyzed in some limited regions (?). Nevertheless, the mechanisms by which land masses alter the seasonal cycle of downwind  
40 oceanic air remain poorly quantified, particularly in the midlatitudes where the jet stream is expected to routinely transport  
41 continental air eastward over the Atlantic and Pacific ocean basins.

42 Understanding the influence of land on the climatological mean state of oceanic air is particularly important given ongoing  
43 changes in continental states. Changes in the land surface alter the climate both locally and globally (Bathiany et al., 2010;  
44 Davin et al., 2010; Kooperman et al., 2017; Laguë et al., 2019); large changes in vegetation can drive atmospheric change over  
45 both land and ocean regions through atmospheric teleconnections and shifts in atmospheric circulation (Bonan, 2008; Bonan  
46 et al., 1992; Laguë and Swann, 2016; Swann et al., 2012). In terrestrial regions with strong land-atmosphere coupling, changes  
47 in soil moisture and vegetation drive changes in precipitation (Koster et al., 2006).

48 The low heat capacity and relative dryness of land causes land to have a large temperature response to thermal forcings,  
49 as evidenced by both the increased variance of land temperature (e.g. seasonally) and the amplified response of land to  
50 heating from increased atmospheric CO<sub>2</sub> (Chadwick et al., 2019; Fu and Feng, 2014; Hartmann, 2015; Sutton et al., 2007).  
51 While increased atmospheric CO<sub>2</sub> over oceans decreases outgoing longwave radiation there, CO<sub>2</sub> increases over land lead

52 to circulation responses which move atmospheric energy from continental to oceanic regions ([Shaw and Voigt, 2016](#)). Plant  
53 responses to CO<sub>2</sub>, changes in soil moisture, growing season timing and length changes, and changes in snow pack lead to  
54 further amplification of continental warming with increased atmospheric CO<sub>2</sub> ([Campbell et al., 2005](#); [Dong et al., 2009](#); [Ipcc, 2022](#)).  
55

56 Here we ask how land influences the seasonal mean state of oceanic air downwind of a continent, using the particular case  
57 of the Atlantic Ocean east of North America; this coastal region is home to numerous large population centers and regions  
58 of high marine productivity. We examine this remote influence of land in the present climate and in projections of changes  
59 resulting from the distinct impacts of CO<sub>2</sub> on atmospheric radiation and on plant physiology.

## 60 **2 Methods**

### 61 **2.1 The land wake**

We define the “land wake”  $W_x$  of some variable  $x$  as the deviation from the zonal mean value of  $x$  of air over the ocean ( $[x_{ocean}]$ ) at a given latitude (equation 1).

$$W_x = x - [x_{ocean}] \quad (1)$$

62  $W_x$  can be calculated globally or for a single ocean basin, at any atmospheric level. We focus on the near-surface wake averaged  
63 from 1000-900 hPa (the precise shape of the wake varies depending on the vertical levels selected), downwind of mid-latitude  
64 North America, where  $[x_{ocean}]$  is averaged longitudinally over the Atlantic ocean, defined here to be the ocean region between  
65 100°W-0°W and 20°N-70°N.  $W_x < 0$  indicates  $x$  at that location is smaller than the average oceanic value of  $x$  for that latitude,  
66 while  $W_x > 0$  indicates  $x$  is larger than the average oceanic value of  $x$  for that latitude. In this study, we focus on the wakes of  
67 relative humidity ( $W_{RH}$ ), specific humidity ( $W_Q$ ), and temperature ( $W_T$ ).

### 68 **2.2 Climate data**

69 We analyse the land wake using a combination of reanalysis data and climate model output. We use the ERA5 reanalysis global  
70 dataset at 0.25° resolution, which spans from 1979-2019 ([Hersbach et al., 2020](#)). Specifically, we use the ERA5 variables for:  
71 relative humidity ( $RH$ ), specific humidity ( $q$ ), temperature ( $T$ ), and winds ( $U, V$ ).

72 We also evaluate the wake in Earth system models under low and high atmospheric CO<sub>2</sub> concentrations. Increased  
73 atmospheric CO<sub>2</sub> has both radiative and biological impacts. These effects are isolated in a pair of experiments from the  
74 Coupled Climate-Carbon Cycle Model Intercomparison Project (C4MIP ([Friedlingstein et al., 2006](#); [Jones et al., 2016](#))). In  
75 “1pctCO<sub>2</sub>-bgc”, only the biogeochemical (bgc) components of the models experience CO<sub>2</sub> increasing at 1% per year from  
76 pre-industrial values (280 ppm), while the atmosphere experiences constant pre-industrial CO<sub>2</sub>. In “1pctCO<sub>2</sub>-rad”, only the  
77 atmospheric radiation experiences increasing CO<sub>2</sub> (at 1% per year), while the biogeochemical components of the model  
78 experience fixed pre-industrial CO<sub>2</sub>. We also consider simulations from the “1pctCO<sub>2</sub>” experiment from the Coupled Model

79 Intercomparison Project v. 6 (Eyring et al., 2016), where both radiation and biogeochemistry experience the increase in CO<sub>2</sub>.  
80 Simulations are run for 140 years, at which point CO<sub>2</sub> concentrations reach 4x pre-industrial levels (Fig. S1). We refer to the  
81 increase in CO<sub>2</sub> experienced by the biogeochemistry as bgcCO<sub>2</sub>, the increase in CO<sub>2</sub> experienced by the atmospheric radiation  
82 as radCO<sub>2</sub>, and use fullCO<sub>2</sub> to refer to simulations where both biogeochemistry and radiation experience increased CO<sub>2</sub>.

83 Both the terrestrial and oceanic carbon cycles experience the increase in bgcCO<sub>2</sub>, but impacts on surface fluxes are only  
84 driven by the response of terrestrial vegetation to increased CO<sub>2</sub>. The bgcCO<sub>2</sub> simulations thus provide a clear demonstration  
85 of changes in land driving changing conditions over the ocean in the land wake. At higher CO<sub>2</sub> concentrations, plants can grow  
86 more (CO<sub>2</sub> fertilization; (Field et al., 1995; Medlyn et al., 2001; Morison, 2001; Sellers et al., 1996)), altering leaf area and land  
87 albedo, in turn leading to changes in surface temperatures and evapotranspiration (Donohue et al., 2013; Swann et al., 2016;  
88 Zariskas et al., 2020a). Atmospheric CO<sub>2</sub> concentrations directly impact the stomatal conductance of vegetation. In global Earth  
89 system models, the equations governing stomatal conductance generate less conductance (thus less evapotranspiration, with all  
90 else held equal) with increased atmospheric CO<sub>2</sub> concentrations (Ball et al., 1987; Medlyn et al., 2011), changing plants' water  
91 use efficiency (Cheng et al., 2014; Eamus, 1991).

92 The effect of the biogeochemical response to increased CO<sub>2</sub> could be obtained by considering results from high-low CO<sub>2</sub>  
93 values in the bgcCO<sub>2</sub> simulations, or by subtracting the radCO<sub>2</sub> simulation from the fullCO<sub>2</sub> simulation. The first gives the  
94 effect of increasing bgcCO<sub>2</sub> in a low-CO<sub>2</sub> climate, while the latter gives the effect of increasing bgcCO<sub>2</sub> in a high-CO<sub>2</sub> climate;  
95 we focus on the first approach in this study, but show that the two methods give generally qualitatively similar responses of the  
96 land wake.

97 We use the 9 models participating in C4MIP that provided temperature, specific humidity, and relative humidity data  
98 for the 1pctCO<sub>2</sub>-bgc and 1pctCO<sub>2</sub>-rad C4MIP experiments and were available for download from the LLNL ESGF node  
99 (<https://esgf-node.llnl.gov/projects/cmip6/>) on August 11, 2021 (table 1). These models were BCC-  
100 CSM2-MR, CanESM5, CNRM-ESM2-1, ACCESS-ESM1-5, IPSL-CM6A-LR, MIROC-ES2L, UKESM1-0-LL, MPI-ESM1-2-  
101 LR, and CESM2. Cloud cover data was available for all models except CanESM5, so low cloud and downwelling solar radiation  
102 are evaluated for the remaining 8 models only; snow cover and leaf area changes are shown for all models except CanESM5  
103 and BCC-CESM2-MR as neither model had both variables available. Where possible, the r1i1p1f1 ensemble member was used,  
104 otherwise the r1i1p1f2 ensemble member was used; only a single ensemble member per model was considered. All output was  
105 re-gridded to a common 1° resolution horizontal grid. For each field considered, we took the difference of the average of years  
106 121-140 (high CO<sub>2</sub>) and subtracted the average of years 1-20 (low CO<sub>2</sub>).

## 107 2.3 Wake magnitude

To compare changes in the *RH* wake in the C4MIP simulations with increased bgcCO<sub>2</sub> and radCO<sub>2</sub>, we define the “magnitude”  
*M* of the wake as the area-weighted sum of the spatial footprint of the Atlantic *RH* wake, in this case, anywhere RH<0,

**Table 1.** C4MIP model simulations used in this study, with data downloaded from the LLNL ESGF node (<https://esgf-node.llnl.gov/projects/cmip6/>) on August 11, 2021. Variables used are: downwelling shortwave radiation (rsds), cloud fraction (cl), winds (ua, va), atmospheric temperature (ta), specific humidity (hus), and relative humidity (hur).

Modeling center	Model name	1pctCO2-bgc ensemble member	1pctCO2-rad ensemble member	Variables assessed
Beijing Climate Center (BCC)	BCC-CSM2-MR	r1i1p1f1	r1i1p1f1	rsds, cl, ua, va, ta, hus, hur
Canadian Centre for Climate Modeling and Analysis (CC-Cma)	CanESM5	r1i1p1f1	r1i1p1f1	ua, va, ta, hus, hur
Centre National de Recherches Météorologiques (CNRM-CERFACS)	CNRM-ESM2-1	r1i1p1f2	r1i1p1f2	rsds, cl, ua, va, ta, hus, hur, snw, tlai
Commonwealth Scientific and Industrial Research Organization (CSIRO)	ACCESS-ESM1-5	r1i1p1f1	r1i1p1f1	rsds, cl, ua, va, ta, hus, hur, snw, tlai
Institut Pierre Simon Laplace (IPSL)	IPSL-CM6A-LR	r1i1p1f1	r1i1p1f1	rsds, cl, ua, va, ta, hus, hur
Model for Interdisciplinary Research on Climate (MIROC)	MIROC-ES2L	r1i1p1f2	r1i1p1f2	rsds, cl, ua, va, ta, hus, hur, snw, tlai
Max Planck Institute for Meteorology (MPI-M)	MPI-ESM1-2-LR	r1i1p1f1	r1i1p1f1	rsds, cl, ua, va, ta, hus, hur, snw, tlai
Met Office Hadley Centre (MOHC)	UKESM1-0-LL	r1i1p1f2	r1i1p1f2	rsds, cl, ua, va, ta, hus, hur, snw, tlai
National Center for Atmospheric Reserach (NCAR)	CESM2	r1i1p1f1	r1i1p1f1	rsds, cl, ua, va, ta, hus, hur, snw, tlai

multiplied by the intensity of the wake  $W_{RH}$ , where  $W_{RH}$  is how negative  $RH$  is at each location:

$$M_{RH,Atlantic} = \frac{\int_{105W}^{25W} \int_{25N}^{65N} (\cos \phi W_{RH})|_{W_{RH} < 0} d\phi d\lambda}{\int_{105W}^{25W} \int_{25N}^{65N} (\cos \phi)|_{W_{RH} < 0} d\phi d\lambda}, \quad (2)$$

where  $\phi$  is the latitude.  $M_{RH,Atlantic}$  is calculated using  $W_{RH}$  in the domain 25–65°N and 105–25°W, only where  $W_{RH}$  is negative. We take the difference of the average monthly  $M_{RH,Atlantic}$  of years 121–140 (high bgcCO<sub>2</sub> and radCO<sub>2</sub>) minus the average monthly  $M_{RH,Atlantic}$  of years 1–20 (low bgcCO<sub>2</sub> and radCO<sub>2</sub>) for the 1pctCO2-bgc and 1pctCO2-rad simulations, respectively. We similarly calculate the change in continental  $RH$  (averaged over land areas from 1000 to 900 hPa, between 25–65°N and 125–55°W) for each month of the year, then take seasonal averages. The wake area changes slightly with increasing bgcCO<sub>2</sub> and radCO<sub>2</sub> (Table S1), but most of the change in the wake magnitude comes from magnitude changes within the climatological wake footprint.

## 2.4 Wake intensity

To evaluate the individual contributions of  $T$  and  $q$  to the change in  $W_{RH}$ , we define an additional metric, the change in the wake “intensity” (equation 3).  $I_{RH}$  is calculated in the box 25–65°N and 105–25°W, *only* where  $\Delta W_{RH} < 0$  (see Fig. 3) for each individual model. Within that footprint, a similar approach is used as with the calculation of the magnitude  $M_{RH}$ , i.e. taking the

area-weighted sum of the wake values in that region (but only where the wake changes, i.e. where  $\Delta W_{RH} < 0$ ).

$$I_{RH} = \frac{\int_{105W}^{25W} \int_{25N}^{65N} (\cos \phi W_{RH})|_{\Delta W_{RH} < 0} d\phi d\lambda}{\int_{105W}^{25W} \int_{25N}^{65N} (\cos \phi)|_{\Delta W_{RH} < 0} d\phi d\lambda}, \quad (3)$$

To separate the impact of  $T$  and  $q$  on  $W_{RH}$ ,  $\Delta W_{RH}$ , and  $I_{RH}$ , we calculate  $W_{RH}$  in three distinct ways. First, we calculate  $W_{RH}$  in the standard manner (equation 1). Second, we calculate what the  $RH$  field would be in the high  $CO_2$  case if we hold  $q$  fixed to the low  $CO_2$  value, but increase  $T$  to the high  $CO_2$  value; we then calculate the wake of that new  $RH$  value that only accounts for the change in  $T$ . Third, we calculate what the  $RH$  field and  $W_{RH}$  would look like with high  $CO_2$  if only  $q$  is increased to high  $CO_2$ , with  $T$  held to the low  $CO_2$  value.  $I_{RH}$  can then be calculated within the  $\Delta W_{RH}$  footprint for low  $CO_2$  (using  $W_{RH}$  at low  $CO_2$ ), for  $RH$  associated with low  $CO_2$   $q$  and high  $CO_2$   $T$ , for  $RH$  associated with low  $CO_2$   $T$  and high  $CO_2$   $Q$ , and for  $RH$  at high  $CO_2$ . These terms do not add linearly as  $RH$  is not a linear function of  $T$  and  $q$  and we approximate the effect of  $\Delta T$  and  $\Delta q$  on  $\Delta RH$  using monthly mean  $T$  and  $q$  values. The actual change in  $RH$  is qualitatively similar but numerically differs slightly from the change in  $RH$  calculated from monthly mean  $T$  and  $q$  together (not shown).

## 2.5 Analysis tools and details

From equation 1, changes in the wake  $W_x$  could occur either because of a change in the spatial pattern of  $x$ , or because of a change in the zonal mean of  $x$  averaged over the Atlantic basin. In the case of increased  $bgcCO_2$ , the changes in the  $RH$  wake are driven by spatial changes in  $RH$  off the North American east coast, with very little change in the zonal mean value of  $RH$  over the Atlantic ocean. This is not surprising, as  $bgcCO_2$  primarily impacts surface energy and water fluxes over the continents; this signal is then advected over the ocean and thus is strongest in the wake region, with very little change in the average Atlantic  $RH$  at each latitude (Fig. S2).

Increasing  $radCO_2$  has a strong impact on the atmospheric radiative budget and surface temperatures over both land and ocean regions, causing the zonal mean Atlantic values of  $T$  and  $q$  to increase, but zonally averaged relative humidity over the ocean remains roughly the same (O’Gorman and Muller, 2010). Regionally however,  $RH$  and the  $RH$  wake become drier with increasing  $radCO_2$  off the North American east coast, as a result of continental warming (Fig. S3).

Western boundary currents, such as the Gulf Stream, cause a tongue of anomalously warm water extending into cooler waters at higher latitudes along the east coast of mid-latitude continents, releasing heat and moisture to the atmosphere above it. In the context of our definition of the wake, this would raise the overall zonally averaged  $RH$ ,  $T$ , and  $q$  of the ocean basin. As such, air that is near the coast but has not yet reached the eastern boundary current could look anomalously cold or dry simply because it has not yet come into contact with the warmer waters. The C4MIP simulations analyzed here show that the  $RH$ ,  $T$ , and  $q$  of the wake region change in response to increased  $bgcCO_2$  and  $radCO_2$ —that is, even if the wake only existed as an artifact of the eastern boundary currents, our analysis still shows the sensitivity of oceanic air in this region to terrestrially-driven changes in continental air. Changes in the location and strength of the Gulf Stream, e.g. with changing climate, could alter both the

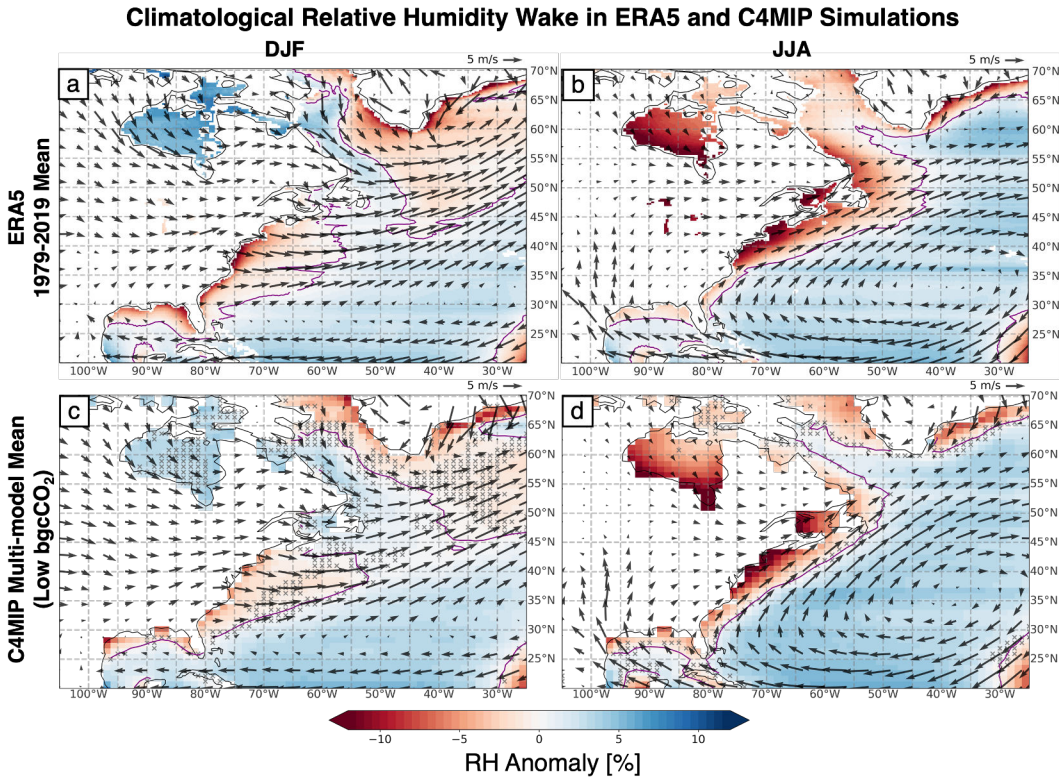


**Figure 1.** The climatological land wake  $W_{RH}$  averaged from 1000-900 hPa, defined as the deviation from zonal-mean ocean relative humidity at each latitude, for DJF (left) and JJA (right). The wake is shown from ERA5 data averaged from 1979-2019 (top) and from the multi-model mean of the first 20 years of the 1pctCO<sub>2</sub>-bgc experiment in 9 C4MIP models (bottom). Arrows show climatological wind vectors averaged from 1000-900 hPa. Hatching on (c,d) indicate regions where less than 6/9 models agree on the sign of the wake. The purple contour indicates the zero line, i.e. the contour of average Atlantic  $RH$  for each latitude.

144 shape and strength of the continental wake by modifying wind patterns and ocean-atmosphere exchange of heat and moisture.  
 145 For example, a warmer gulf stream could potentially reduce the continental wake as increased ocean evaporation could more  
 146 quickly make continental air resemble ocean air.

147 Analysis was conducted using the Python programming language, heavily leveraging the NumPy ([Harris et al., 2020](#)) and  
 148 xarray ([Hoyer and Hamman, 2017](#)) packages.

### 149 3 Results

#### 150 3.1 The present-day land wake and its causes

151 In reanalysis data,  $W_{RH}$  downwind of mid-latitude North America is negative in both winter (December-February, DJF) and  
 152 summer (June-August, JJA), becoming positive as air moves further from shore (Fig. 1a,b); that is, air near the continent has a  
 153 lower relative humidity (RH) than air farther from land. The shape of the wake changes with season, but its longest dimension  
 154 is generally aligned parallel to the time-mean low-level wind with a peak length of at least 1,000 km. In winter,  $W_{RH}$  extends  
 155 from the northern coast of the Gulf of Mexico along the eastern seaboard of the USA to around 50°N, with an additional region

156 of anomalously low  $RH$  around Greenland (Fig. 1a). In summer, the wake lies closer to shore along the east coast of the USA,  
157 but extends further north along the east coast of Canada and Hudson Bay, while the Greenland wake retreats towards the coast  
158 of that land mass (Fig. 1b). Eastward winds off the continent are stronger in winter, and the winter wake correspondingly  
159 extends farther from shore between 30–45°N. In contrast, the summer wake is more intense and occupies a larger fraction of the  
160 coastline of North America.

161 While the  $RH$  wake is apparent in both winter and summer, it is driven by different mechanisms seasonally. In winter, cold,  
162 dry air flows from the continent over ocean, producing low temperature ( $T$ ) and low specific humidity ( $q$ ) offshore (Fig. 2a,c).  
163 However, because saturation vapor pressure decreases rapidly as temperature drops, the low temperatures in more northern  
164 regions prevent anomalously low  $RH$  downwind of the continent. The winter wakes in  $T$  and  $q$  extend along nearly the entire  
165 coastline of North America, but their interaction limits the  $RH$  wake to latitudes south of Nova Scotia (Fig. 1a). In summer,  
166 time-mean winds along eastern North America flow more parallel to the coast due to the summertime anticyclone over the  
167 Atlantic (Fig. 1b). At more southern latitudes,  $q$  is anomalously positive due to moisture transport from the low-latitude ocean,  
168 while at more northern latitudes  $q$  is anomalously negative where there is flow off the continent (Fig. 2b). Close to the continent,  
169 air is warmer than average ocean air (Fig. 2d); as in winter, the shape of  $W_{RH}$  results from the strong response of saturation  
170 vapor pressure to temperature, yielding low  $RH$  along the whole east coast of North America despite anomalously high  $q$  south  
171 of 40°N (Fig. 1b, 2b).

172 Mixing between continental and maritime regions produced by shorter timescale motions and vertical circulations is likely  
173 also a factor in determining the wake. For example, along the northern coast of the Gulf of Mexico, monthly mean winds are  
174 climatologically onshore, yet a distinct band of low RH air hugs the coast. The difference in seasonal drivers of  $W_{RH}$  illustrate  
175 the potential for long-term changes to land, such as those caused by agriculture, fire, drought, and rising atmospheric CO<sub>2</sub>, to  
176 impact ocean regions downwind of continents through multiple mechanisms.

### 177 3.2 Intensification of the land wake by increased CO<sub>2</sub>

178 Temperature increases due to climate change are occurring more quickly over land than over most ocean regions (IPCC, 2007),  
179 and the existence of the land wake provides a pathway for land's response to climate change to influence ocean regions. Earth  
180 System Models (ESMs) participating in C4MIP produce a qualitatively similar  $W_{RH}$  to that seen in reanalysis (cf. top and  
181 bottom rows of Fig. 1), with the ERA5 wake having a slightly larger area than the models (Table S1).

182 Increases in bgcCO<sub>2</sub> and radCO<sub>2</sub> each separately strengthen the land wake (Fig. 3). The spatially integrated magnitude of  
183 the relative humidity wake ( $M_{RH,Atlantic}$ , see Methods) intensifies in response to both increased bgcCO<sub>2</sub> and radCO<sub>2</sub>, with both  
184 driving similar magnitudes of change in  $M_{RH,Atlantic}$  during summer (Fig. 4a,b). This intensification of the wake accompanies  
185 a large reduction of  $RH$  over continental North America during spring, summer, and autumn (Fig. 4), although the spring  
186 and autumn changes are less pronounced in the radCO<sub>2</sub> experiment. There is a strong correlation across models ( $r^2 = 0.72$ )  
187 between the change in  $RH$  over North America and the change in the  $RH$  wake magnitude associated with increased bgcCO<sub>2</sub>,  
188 and a more modest correlation ( $r^2 = 0.57$ ) for radCO<sub>2</sub>. These results support the hypothesis that changes in continental air

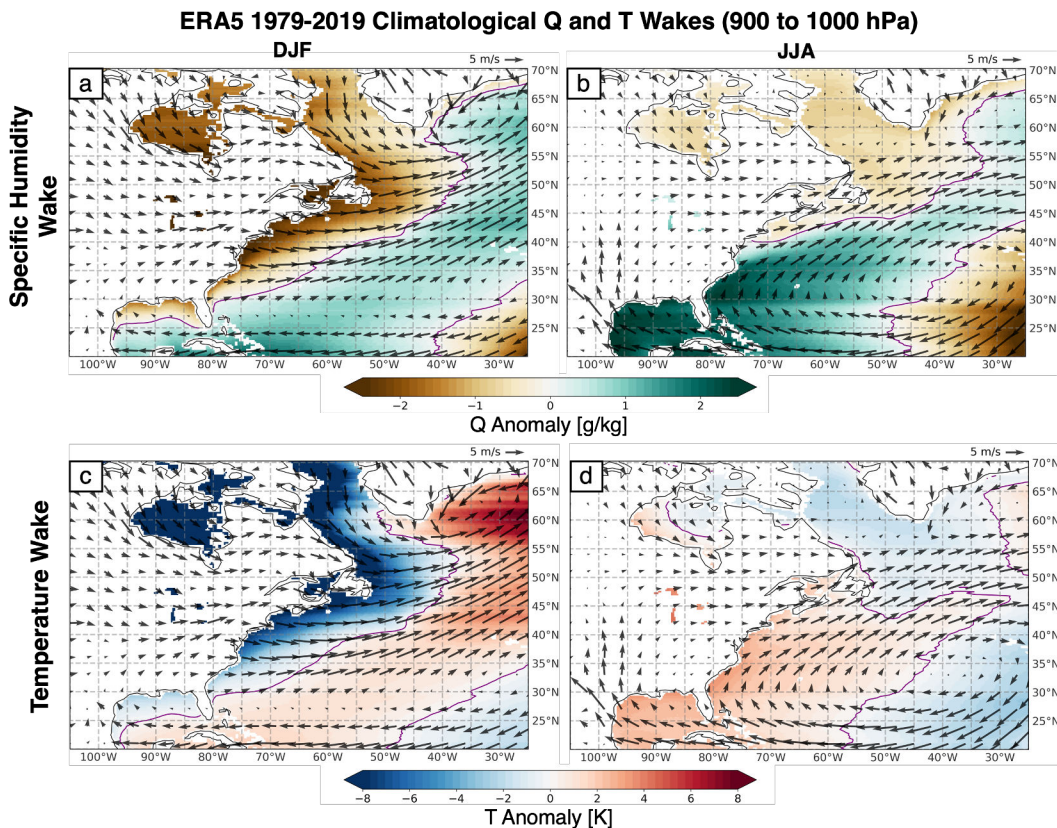


**Figure 2.** The climatological land wakes  $W_Q$  (top) and  $W_T$  (bottom), averaged from 1000-900 hPa, for DJF (left) and JJA (right), for ERA5 data averaged from 1979-2019. Arrows show climatological wind vectors averaged from 1000-900 hPa. The purple contour indicates the zero line, i.e. the contour of average Atlantic  $q$  or  $T$  for each latitude.

189 induced by the radiative and biogeophysical effects of CO<sub>2</sub> drive changes in the wake.

190 When radiative and biogegeochemical effects of CO<sub>2</sub> are both considered (using the fullCO<sub>2</sub> simulations), the radCO<sub>2</sub> effects  
191 are seen to dominate the spatial pattern change in the wake found in the fullCO<sub>2</sub> simulation (Fig. 3). However, the effects of  
192 bgcCO<sub>2</sub> contribute substantial changes to the wake magnitude (Fig. 4c). We would not expect the wake changes in the bgcCO<sub>2</sub>  
193 and radCO<sub>2</sub> simulations to sum perfectly linearly to the fullCO<sub>2</sub> wake change because the results of the ΔbgcCO<sub>2</sub> simulations  
194 show the effect of bgcCO<sub>2</sub> in a low-CO<sub>2</sub> background climate, while the difference between the fullCO<sub>2</sub>-radCO<sub>2</sub> simulations  
195 show the effect of bgcCO<sub>2</sub> in a high-CO<sub>2</sub> background climate. However, the full–rad wake response is qualitatively similar to  
196 the bgcCO<sub>2</sub> wake response in most regions, except in the Hudson Bay and Davis Straight areas (Figs. S4–S6). These differences  
197 are not the focus of our study, but we suspect they result from large differences in base-state Arctic climate with low vs. high  
198 CO<sub>2</sub>.

### 199 **3.3 Biogeophysical effects of CO<sub>2</sub> intensify wake through stomatal closure**

200 We now focus on how the response of terrestrial evapotranspiration to increased bgcCO<sub>2</sub> impacts the wake. The summer  
201 response across the C4MIP simulations to increased bgcCO<sub>2</sub> is a widespread reduction in terrestrial evapotranspiration (Fig. S7).  
202 The terrestrial biogeophysical effects of increased CO<sub>2</sub> produce a wake that is drier (i.e.  $W_{RH}$  is anomalously low) over the  
203 coastal ocean in both summer and winter with increased bgcCO<sub>2</sub> (Fig. 3a, b). Note that though the RH wake becomes drier,  
204 specific humidity in the summer wake actually increases because of circulation changes, discussed below. While the horizontal  
205 extent of this change in the wake is smaller in summer, the peak intensity (defined by eq. 3) of this change is larger during  
206 that season. Although the definition of  $W$  (eq. 1) encompasses the whole Atlantic, the change in  $W_{RH}$  is primarily the result of  
207 changes near North America, with little influence from the zonal-mean change (Figs. S2, S7; see Methods for further discussion).

208 In summer, continental  $RH$  decreases as a result of reduced continental evapotranspiration driven by the stomatal response  
209 to increased bgcCO<sub>2</sub>, but the influence of these continental changes on the  $RH$  wake is more complex than a simple downwind  
210 transport of low- $RH$  air. The reduced continental evapotranspiration causes lower continental  $q$  as well as higher continental  
211  $T$  due to reduced latent cooling of land (see land regions in Figs. 3b and S7b,d). Downwind transport of high- $T$  air over the  
212 wake region drives an intensification of the  $RH$  wake, but this is partially opposed by an increase in  $q$  over much of the western  
213 Atlantic (Fig. S7b,d). Because continental  $q$  decreases with increased bgcCO<sub>2</sub>, the downwind transport of lower  $q$  continental  
214 air cannot explain the summer increase in  $q$  in the wake region. Summer ocean evaporation also does not change substantially  
215 in the wake region (Fig. S8). Instead, the increase in summer  $q$  over the western Atlantic is due to a change in atmospheric  
216 circulation. The continental warming resulting from reduced evapotranspiration induces an anomalous low-level cyclone  
217 centered over the eastern edge of the continent, bringing warm, moist air from the Gulf of Mexico and Caribbean northward  
218 along the coast of North America (Fig. S9). The transport of moisture into the wake region by this anomalous circulation damps  
219 the temperature-induced intensification of the  $RH$  wake. The combination of the opposing effects of the  $T$  and  $q$  changes on  
220  $RH$  produces a slight intensification of the  $RH$  wake with increased bgcCO<sub>2</sub> across all models (Fig. 5).

221 The drivers of winter  $W_{RH}$  change are different than those in summer. In winter, there is little change in continental  $RH$ ,

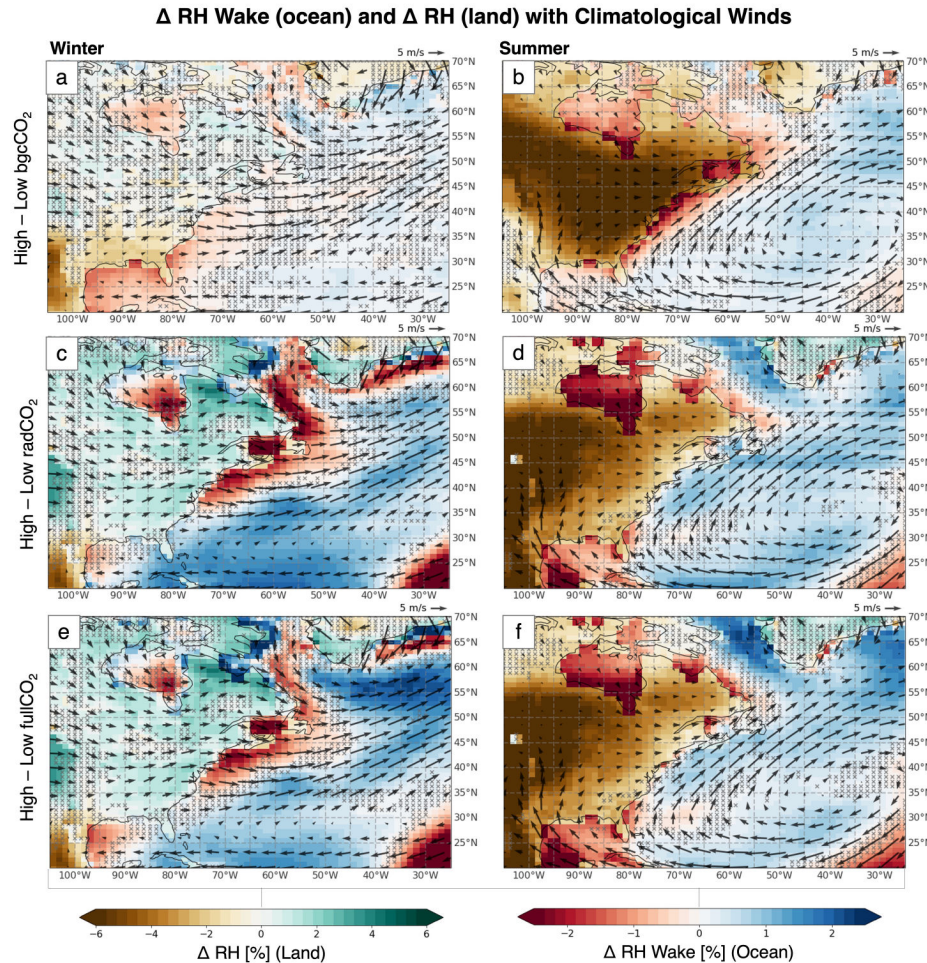


**Figure 3.** Change (high - low  $\text{CO}_2$ ) in the  $\text{RH}$  land wake for the difference of the end-start of the C4MIP simulations where only the carbon cycle sees increased  $\text{bgcCO}_2$  (top), only radiation sees increased  $\text{radCO}_2$  (middle), and both  $\text{bgc}$  and radiation see increased  $\text{CO}_2$  (bottom) for winter (left) and summer (right). Negative values indicate a “drying” (lower  $\text{RH}$ ) of the wake. Hatching indicates where less than 7/9 models agree on the sign of the response. The change in  $\text{RH} [\%]$  is shown over land, with change in the  $\text{RH Wake} [\%]$  over the ocean. Wake values and continental  $\text{RH}$  are averaged from the surface to 900 hPa. Vectors show climatological winds averaged from 1000 to 900 hPa.

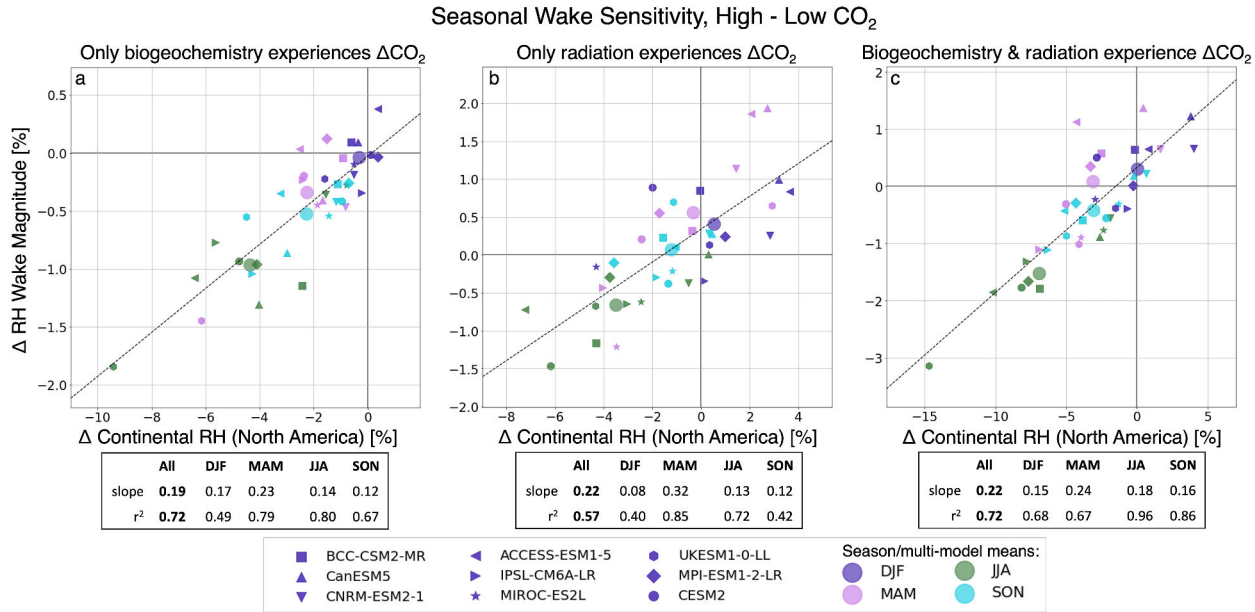


**Figure 4.** The relationship between the change in continental RH and the magnitude ( $M_{RH}$  = footprint  $\times$  intensity) of the relative humidity wake for high - low CO<sub>2</sub> where (a) only bgc, (b) only radiation, and (c) both bgc and radiation experience the ΔCO<sub>2</sub>, where negative values mean a lower relative humidity. Continental RH is averaged from the surface to 900 hPa over land areas from 25°–65°N and 125°–55°W. Individual models are each identified with their own marker, while the large circles show the multi-model mean; colors indicate season. The black dashed line shows the line of best fit to all points; the slope and  $r^2$  value for all points and the points in each season are noted below each panel. Note the axis ranges differ across panels.

but  $W_{RH}$  still intensifies (Fig. 3). Rather than being driven directly by downwind transport of anomalous continental RH, the reduction in winter  $W_{RH}$  is due to increased continental temperatures, which are caused by a darker land surface resulting from reduced snow cover and increased winter leaf area (Figs. S7, S10). The darkened land surface absorbs more shortwave energy, leading to warming of the surface and overlying atmosphere in the winter.

### 3.4 Radiative effects of CO<sub>2</sub> intensify wake through continental warming

The radiative effects of enhanced CO<sub>2</sub> intensify  $W_{RH}$  in both winter and summer, but with spatial patterns and magnitudes that differ greatly from those caused by the biogeophysical effects of CO<sub>2</sub> (Fig. 3). The intensification of  $W_{RH}$  with increased radCO<sub>2</sub> results from the radiatively driven increase in land surface temperatures (Fig. S11). In contrast to increased bgcCO<sub>2</sub>, which has the largest impact on temperatures over land, increased radCO<sub>2</sub> drives widespread warming over both land and ocean, with stronger warming than bgcCO<sub>2</sub>; the hotter atmosphere has a greater evaporative demand and causes increased terrestrial evapotranspiration in many regions (Fig. S11). This response of evapotranspiration is not large enough to fill the enhanced vapor pressure deficit that drives it, so the large increase in land temperatures produces a decrease in summer continental RH and an intensification of  $W_{RH}$ . As in the bgcCO<sub>2</sub> case,  $q$  increases in the region where  $W_{RH}$  intensifies as a result of anomalous poleward winds over the western Atlantic, but for radCO<sub>2</sub> this poleward flow is part of an anomalous anticyclone centered over Florida and the Gulf of Mexico (Fig. S9). On its own, this increase in  $q$  would lead to a weaker  $W_{RH}$ , while the increase in  $T$  would lead to a strong intensification of  $W_{RH}$  (Fig. 5). The final result is a modest intensification of the wake as a result of

### Decomposition of Summer $\Delta$ Wake Intensity into Contributions from $\Delta T$ and $\Delta Q$

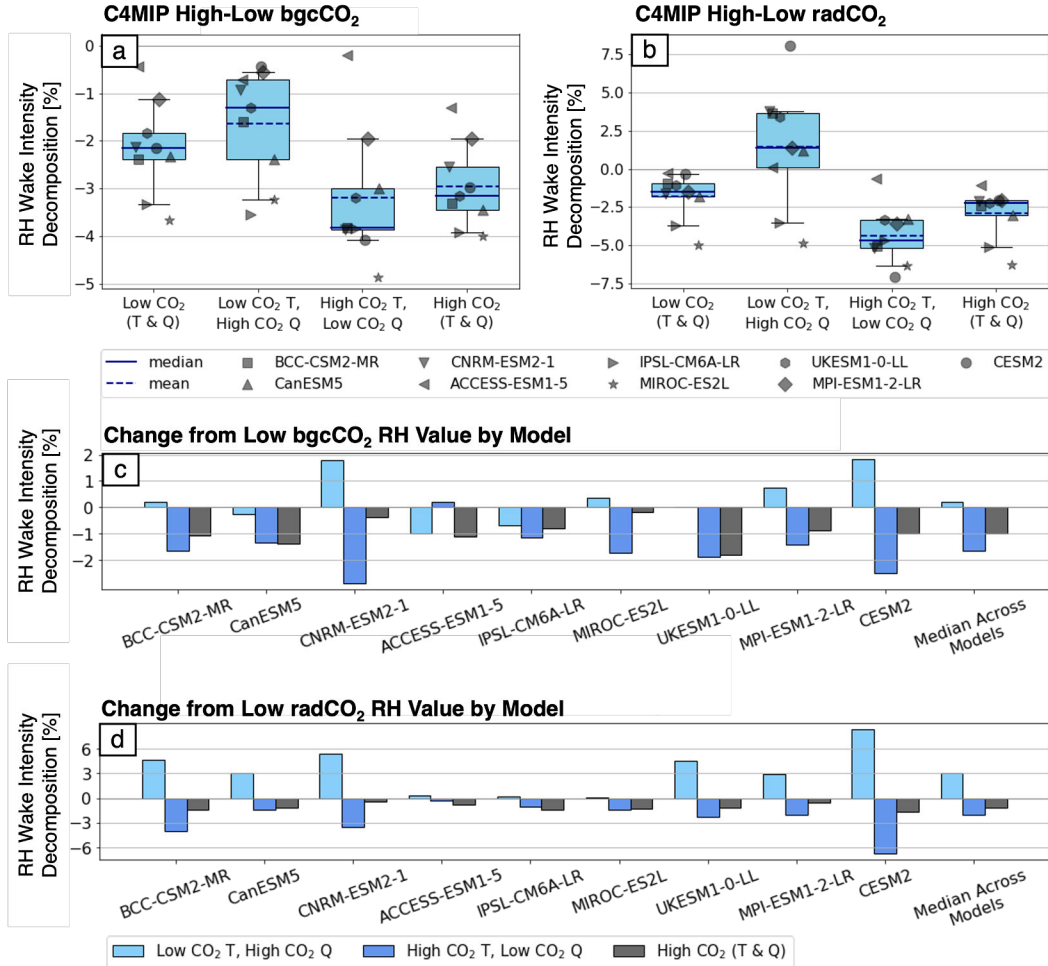


**Figure 5.** Summer  $RH$  wake intensity change decomposed into contributions from changes in  $T$  and changes in  $q$  in the region of the  $RH$  wake intensification with increased (a)  $bgcCO_2$  and (b)  $radCO_2$ , where positive values correspond to higher (moister)  $RH$  and negative values correspond to lower (drier)  $RH$ . Panels c & d show the change in the  $RH$  wake from the low  $CO_2$  wake value in for each model, for  $bgcCO_2$  and  $radCO_2$  respectively.

## Change in summer low cloud cover and downwelling shortwave radiation with increased bgcCO<sub>2</sub>

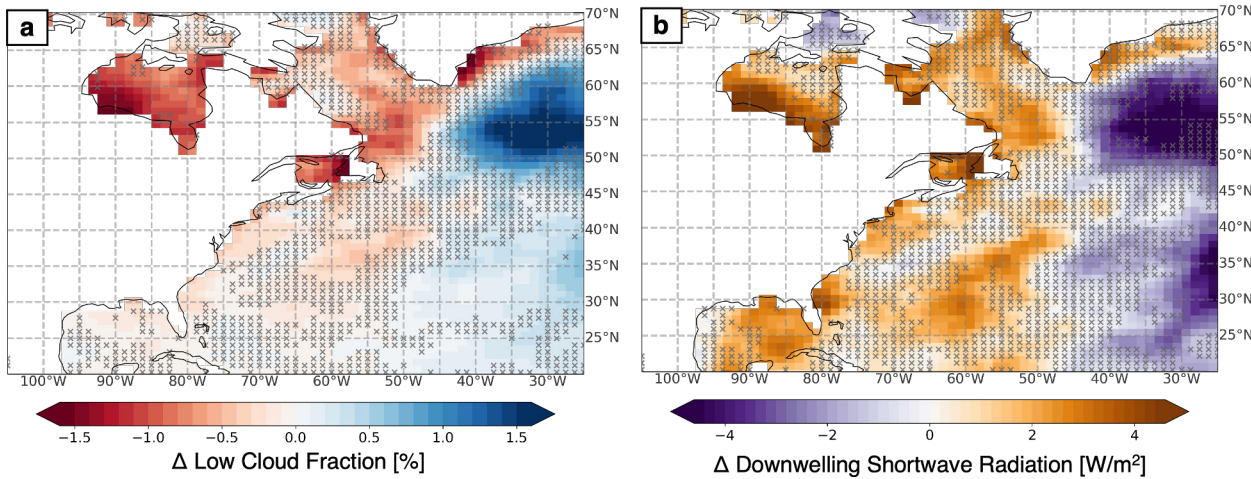


**Figure 6.** Change in summer low cloud fraction (left, %) and downwelling shortwave radiation at the surface (right, W/m<sup>2</sup>) with increased bgcCO<sub>2</sub>. Hatching indicates where less than 6/8 models agree on the sign of the response. “Low clouds” are considered to be clouds from the surface to 700 hPa for models that report cloud fraction on pressure coordinates, and from the surface to 3000 m for models that report cloud fraction on height coordinates.

increased radCO<sub>2</sub>.

While the peak magnitude of the wintertime  $W_{RH}$  change is more than twice as large for radCO<sub>2</sub> than for bgcCO<sub>2</sub>, the wake change induced by bgcCO<sub>2</sub> occupies a larger spatial area (c.f. Figs. 3a, c). In summer, the radCO<sub>2</sub> wake changes are largest in Hudson Bay and the Gulf of Mexico, while for bgcCO<sub>2</sub> the changes occur largely along the eastern seaboard of Canada and the USA, suggesting that future plant changes driven by the biogeophysical effects of CO<sub>2</sub> will dominate changes in the wake from Florida to Newfoundland.

### 3.5 Implications for coastal clouds and radiation

Increased CO<sub>2</sub> drives changes not only in coastal RH, but in coastal cloud cover and radiation. With increased bgcCO<sub>2</sub>, summer low cloud cover decreases along the full length of North America’s east coast, from the Gulf of Mexico to Hudson Bay (Fig. 6a). The reduced cloud fraction occurs year-round, with some seasonal changes in structure; cloud loss in the Gulf of Mexico is largest in winter (not shown), while cloud loss in Hudson Bay is largest in summer. Co-located with the reduction in low cloud cover is an increase of roughly 3 W/m<sup>2</sup> in downwelling shortwave radiation (Fig. 6b). Coastal low cloud cover is also reduced as a result of increased radCO<sub>2</sub>, though for that forcing the total change in downwelling shortwave radiation at the surface is complicated by the response of clouds and other absorbers to the radiative effects of CO<sub>2</sub> (not shown).

## 4 Discussion

The reduction in coastal cloud cover with increased bgcCO<sub>2</sub> is notable as the North American east coast is host to large human population centers and important marine ecosystems, in an area already prone to episodic clear-sky coastal events (Fig. S12). The changes in clouds directly alter the amount of sunlight reaching the ocean surface in these high-productivity coastal areas;

256 while these regions are largely nutrient limited, they also experience seasonal light limitation ([Arteaga et al., 2014](#)) and have  
257 high chlorophyll concentrations ([Gregg et al., 2005](#)). Thus, the response of the terrestrial carbon cycle to increased bgcCO<sub>2</sub>  
258 could, by altering downwelling shortwave radiation in the land wake region, impact ocean biogeochemistry.

259 Independent of its effects on ocean biology, increased ocean surface shortwave radiation also has implications for sea surface  
260 temperatures. While these changes in coastal cloud fraction and downwelling shortwave radiation are modest in magnitude,  
261 they represent an as-yet unidentified mechanism through which terrestrial processes—i.e. the plant response to bgcCO<sub>2</sub>—can  
262 alter ocean processes by causing atmospheric change.

263 The biogeochemically induced changes in the land wake presented here represent a new mechanism of regional climate  
264 change. The radiative effects of increased atmospheric CO<sub>2</sub> on atmospheric water vapor and cloud cover have been widely  
265 examined, yet continue to be a large source of uncertainty for future climate projections ([Ceppi et al., 2017](#); [Held and Soden,](#)  
266 [2000](#); [Kärcher, 2017](#); [Lohmann, 2006](#); [Sherwood et al., 2010](#); [Stephens, 2005](#); [Wood, 2012](#)). The land wake represents a  
267 non-local climate response driven by the advection of air carrying a continental signature over ocean regions. This is distinct  
268 from changes in terrestrial climate driven by plant responses to CO<sub>2</sub> (e.g. [Swann et al. \(2016\)](#); [Zarakas et al. \(2020b\)](#)) or  
269 vegetation change (e.g. [Kleidon et al. \(2000\)](#)), and distinct from large scale circulation-inducing ecoclimate teleconnections  
270 (e.g. [Garcia et al. \(2016\)](#); [Laguë \(2016\)](#); [Swann et al. \(2012\)](#)).

271 The remote influence of continental biogeophysical and biogeochemical changes on oceanic air likely involve a related set  
272 of complex processes, with the changes in coastal temperatures and humidities coupled to the Plank, water vapor, and lapse rate  
273 feedbacks ([Laguë et al., 2021](#); [Soden and Held, 2006](#)). These processes merit further exploration, in the context of both forced  
274 long-term climate change and ongoing interannual variability.

275 Future study could also explore how extreme continental drought, heat waves, irrigation, and agriculture impact the land  
276 wake downwind of North America and other continents, and how terrestrially-driven atmospheric changes over ocean regions  
277 downwind of the continents impact ocean processes and productivity. The sensitivity of the wake to land-atmosphere coupling  
278 has yet to be explored. We might expect changes in terrestrial processes in regions with weak land-atmosphere coupling  
279 (e.g. as defined in [Koster et al. \(2006\)](#)) to have less impact on the continental wake than changes in terrestrial regions with  
280 strong land-atmosphere coupling. Further study should focus on which continental regions have the strongest control on the  
281 continental wake.

282 While this study focused on the Atlantic wake east of North America, similar mid-latitude wakes exist off the east coasts of  
283 Asia and South America (not shown). Asymmetries in RH also occur at lower latitudes, co-located with the subtropical cloud  
284 decks; further study is required to determine the relative contributions of ocean upwelling, atmospheric subsidence, clouds, and  
285 continental advection in these climatically important regions. Reanalysis data could be leveraged to explore the interannual  
286 variability of the wake and determine its sensitivity to large-scale climate modes of variability.

287

288 **Acknowledgements**

289 This research used resources of the National Energy Research Scientific Computing Center (NERSC), a U.S. Department of  
290 Energy Office of Science User Facility located at Lawrence Berkeley National Laboratory, operated under Contract No. DE-  
291 AC02-05CH11231. We acknowledge high-performance computing support from Cheyenne (doi:10.5065/D6RX99HX) provided  
292 by NCAR's Computational and Information Systems Laboratory, sponsored by the National Science Foundation, and the data  
293 access and computing support provided by the NCAR CMIP Analysis Platform (doi:10.5065/D60R9MSP). We acknowledge  
294 the World Climate Research Programme, which, through its Working Group on Coupled Modelling, coordinated and promoted  
295 CMIP6. We thank the climate modeling groups for producing and making available their model output, the Earth System Grid  
296 Federation (ESGF) for archiving the data and providing access, and the multiple funding agencies who support CMIP6 and  
297 ESGF. We acknowledge the use of imagery from the NASA Worldview application (<https://worldview.earthdata.nasa.gov/>),  
298 part of the NASA Earth Observing System Data and Information System (EOSDIS). M.M.L. acknowledges funding support  
299 from the James S. McDonnell Foundation Postdoctoral Fellowship in Dynamic and Multiscale Systems. W.R.B. acknowledges  
300 support by the U.S. Department of Energy, Office of Science, Office of Biological and Environmental Research, Climate and  
301 Environmental Sciences Division, Regional and Global Model Analysis Program, under Award DE-SC0019367.

302 **Data availability**

303 ERA5 and C4MIP data are publicly available from [https://cds.climate.copernicus.eu/#!/search?text=](https://cds.climate.copernicus.eu/#!/search?text=ERA5&type=dataset)  
304 [ERA5&type=dataset](https://esgf-node.llnl.gov/projects/cmip6/) and <https://esgf-node.llnl.gov/projects/cmip6/>, respectively. Scripts used in the  
305 analysis, including the python environment used for analysis, are available on github at [https://github.com/marysa/](https://github.com/marysa/LandWake)  
306 [LandWake](https://github.com/marysa/LandWake).

307 **Author contributions statement**

308 M.M.L. came up with the initial project idea, performed model simulations, and conducted the analysis. All authors discussed  
309 the analysis, suggested ideas for exploration, and contributed to the manuscript.

310 **References**

311 Lionel Arteaga, Markus Pahlow, and Andreas Oschlies. Global patterns of phytoplankton nutrient and light colimitation  
312 inferred from an optimality-based model. *Global Biogeochemical Cycles*, 28(7):648–661, 2014. ISSN 19449224. doi:  
313 10.1002/2013GB004668.

314 J Timothy Ball, Ian E Woodrow, and Joseph A Berry. A Model Predicting Stomatal Conductance and Its Contribution to the  
315 Control of Photosynthesis Under Different Environmental Conditions. *Progress in Photosynthesis Research*, (January), 1987.  
316 doi: 10.1007/978-94-017-0519-6. ISBN: 9789401705196.

- 317 Sebastian Bathiany, M Claussen, V Brovkin, T Raddatz, and V Gayler. Combined biogeophysical and biogeochemical effects  
318 of large-scale forest cover changes in the MPI earth system model. *Biogeosciences*, 7(5):1383–1399, 2010. ISSN 17264170.  
319 doi: 10.5194/bg-7-1383-2010. Publisher: Copernicus GmbH ISBN: 1726-4170.
- 320 Gordon B. Bonan. Forests and climate change: Forcings, feedbacks, and the climate benefits of forests. *Science*, 320(5882):  
321 1444–1449, 2008. ISSN 00368075. doi: 10.1126/science.1155121.
- 322 Gordon B Bonan, David Pollard, and Starley L Thompson. Effects of boreal forest vegetation on global climate. *Nature*, 359  
323 (6397):716–718, 1992. ISSN 0028-0836. doi: Doi10.1038/359716a0. ISBN: 0028-0836.
- 324 William R. Boos and Zhiming Kuang. Sensitivity of the South Asian monsoon to elevated and non-elevated heating. *Scientific  
325 Reports*, 3:3–6, 2013. ISSN 20452322. doi: 10.1038/srep01192.
- 326 Cletus J. Burke. Transformation of Polar Continental Air to Polar Maritime Air. *Journal of Meteorology*, 2(2):94–112, 1945.  
327 doi: [https://doi.org/10.1175/1520-0469\(1945\)002<0094:TOPCAT>2.0.CO;2](https://doi.org/10.1175/1520-0469(1945)002<0094:TOPCAT>2.0.CO;2).
- 328 Steven Businger and Richard J. Reed. Cyclogenesis in Cold Air Masses. *Weather and Forecasting*, 4(2):133–156, June 1989.  
329 ISSN 1520-0434, 0882-8156. doi: 10.1175/1520-0434(1989)004<0133:CICAM>2.0.CO;2. URL [https://journals.ametsoc.org/view/journals/wefo/4/2/1520-0434\\_1989\\_004\\_0133\\_cicam\\_2\\_0\\_co\\_2.xml](https://journals.ametsoc.org/view/journals/wefo/4/2/1520-0434_1989_004_0133_cicam_2_0_co_2.xml). Pub-  
330 lisher: American Meteorological Society Section: Weather and Forecasting.
- 331 John L. Campbell, Myron J. Mitchell, Peter M. Groffman, Lynn M. Christenson, and Janet P. Hardy. Winter in northeastern  
332 North America: a critical period for ecological processes. *Frontiers in Ecology and the Environment*, 3(6):314–322, August  
333 2005. ISSN 1540-9295. doi: 10.1890/1540-9295(2005)003[0314:WINNAA]2.0.CO;2. URL [http://doi.wiley.com/10.1890/1540-9295\(2005\)003\[0314:WINNAA\]2.0.CO;2](http://doi.wiley.com/10.1890/1540-9295(2005)003[0314:WINNAA]2.0.CO;2).
- 334 Toby N. Carlson and Joseph M. Prospero. The Large-Scale Movement of Saharan Air Outbreaks over the Northern Equatorial  
335 Atlantic. *Journal of Applied Meteorology*, 11(March):283–297, 1972. doi: [https://doi.org/10.1175/1520-0450\(1972\)011<0283:TLSMOS>2.0.CO;2](https://doi.org/10.1175/1520-0450(1972)011<0283:TLSMOS>2.0.CO;2).
- 336 Paolo Ceppi, Florent Brient, Mark D. Zelinka, and Dennis L. Hartmann. Cloud feedback mechanisms and their representation  
337 in global climate models. *Wiley Interdisciplinary Reviews: Climate Change*, 8:e465:1–21, 2017. ISSN 17577799. doi:  
338 10.1002/wcc.403.
- 342 Robert D Cess and Steven D Goldenberg. The effect of ocean heat capacity upon global warming due to increasing atmospheric  
343 carbon dioxide. *Journal of Geophysical Research*, 86(80):498–502, 1981.
- 344 Robin Chadwick, Duncan Ackerley, Tomoo Ogura, and Dietmar Dommegget. Separating the Influences of Land Warming,  
345 the Direct CO<sub>2</sub> Effect, the Plant Physiological Effect, and SST Warming on Regional Precipitation Changes. *Journal of  
346 Geophysical Research: Atmospheres*, 124(2):624–640, 2019. ISSN 21698996. doi: 10.1029/2018JD029423.

- 347 Lei Cheng, Lu Zhang, Ying-Ping Wang, Qiang Yu, and Derek Eamus. Quantifying the effects of elevated CO<sub>2</sub> on water  
348 budgets by combining FACE data with an ecohydrological model: QUANTIFYING THE EFFECTS OF ELEVATED CO<sub>2</sub>  
349 ON WATER BUDGETS. *Ecohydrology*, 7(6):1574–1588, December 2014. ISSN 19360584. doi: 10.1002/eco.1478. URL  
350 <https://onlinelibrary.wiley.com/doi/10.1002/eco.1478>.
- 351 Kerry H. Cook and Isaac M. Held. The Stationary Response to Large-Scale Orography in a General Circulation Model and a  
352 Linear Model. *Journal of the Atmospheric Sciences*, 49(9):525–539, 1992. doi: [https://doi.org/10.1175/1520-0469\(1992\)049<0525:TSRTLS>2.0.CO;2](https://doi.org/10.1175/1520-0469(1992)049<0525:TSRTLS>2.0.CO;2).
- 354 Edouard L. Davin, Nathalie de Noblet-Ducoudré, Nathalie de Noblet-Ducoudre, and Nathalie de Noblet-Ducoudré. Climatic  
355 Impact of Global-Scale Deforestation: Radiative versus Nonradiative Processes. *Journal of Climate*, 23(1):97–112, January  
356 2010. ISSN 0894-8755. doi: 10.1175/2009JCLI3102.1.
- 357 Buwen Dong, Jonathan M. Gregory, and Rowan T. Sutton. Understanding Land–Sea Warming Contrast in Response to  
358 Increasing Greenhouse Gases. Part I: Transient Adjustment. *Journal of Climate*, 22(11):3079–3097, June 2009. ISSN  
359 1520-0442, 0894-8755. doi: 10.1175/2009JCLI2652.1. URL <http://journals.ametsoc.org/doi/10.1175/2009JCLI2652.1>.
- 361 Randall J. Donohue, Michael L. Roderick, Tim R. McVicar, and Graham D. Farquhar. Impact of CO<sub>2</sub> fertilization on maximum  
362 foliage cover across the globe's warm, arid environments. *Geophysical Research Letters*, 40(12):3031–3035, 2013. ISSN  
363 00948276. doi: 10.1002/grl.50563.
- 364 D. Eamus. The interaction of rising CO<sub>2</sub> and temperatures with water use efficiency. *Plant, Cell and Environment*, 14  
365 (8):843–852, October 1991. ISSN 0140-7791, 1365-3040. doi: 10.1111/j.1365-3040.1991.tb01447.x. URL <https://onlinelibrary.wiley.com/doi/10.1111/j.1365-3040.1991.tb01447.x>.
- 367 Veronika Eyring, Sandrine Bony, Gerald A. Meehl, Catherine A. Senior, Bjorn Stevens, Ronald J. Stouffer, and Karl E.  
368 Taylor. Overview of the Coupled Model Intercomparison Project Phase 6 (CMIP6) experimental design and organization.  
369 *Geoscientific Model Development*, 9(5):1937–1958, 2016. ISSN 19919603. doi: 10.5194/gmd-9-1937-2016.
- 370 C. B. Field, R. B. Jackson, and H. A. Mooney. Stomatal responses to increased CO<sub>2</sub>: implications from the plant to the global  
371 scale. *Plant, Cell & Environment*, 18(10):1214–1225, 1995. ISSN 13653040. doi: 10.1111/j.1365-3040.1995.tb00630.x.
- 372 P Friedlingstein, P Cox, R Betts, L Bopp, W von Bloh, V Brovkin, P Cadule, S Doney, M Eby, I Fung, G Bala, J John,  
373 C Jones, F Joos, T Kato, M Kawamiya, W Knorr, K Lindsay, H D Matthews, T Raddatz, P Rayner, C Reick, E Roeckner,  
374 K.-G. Schnitzler, R Schnur, K Strassmann, a. J Weaver, C Yoshikawa, and N Zeng. Climate–Carbon Cycle Feedback  
375 Analysis: Results from the C 4 MIP Model Intercomparison. *Journal of Climate*, 19(14):3337–3353, 2006. ISSN 0894-8755.  
376 doi: 10.1175/JCLI3800.1. URL <http://journals.ametsoc.org/doi/abs/10.1175/JCLI3800.1>. ISBN:  
377 0894-8755.

- 378 Jiangping Fu, Bo Wang, Ying Chen, and Qingwei Ma. The influence of continental air masses on the aerosols and nutrients  
379 deposition over the western North Pacific. *Atmospheric Environment*, 172(October 2017):1–11, 2018. ISSN 18732844. doi:  
380 10.1016/j.atmosenv.2017.10.041.
- 381 Qiang Fu and Song Feng. Responses of terrestrial aridity to global warming. *Journal of Geophysical Research: Atmospheres*,  
382 pages 7863–7875, 2014. ISSN 00280836. doi: 10.1002/2014JD021608.
- 383 Julia Fuchs, Jan Cermak, Hendrik Andersen, Rainer Hollmann, and Katharina Schwarz. On the Influence of Air Mass Origin  
384 on Low-Cloud Properties in the Southeast Atlantic. *Journal of Geophysical Research Atmospheres*, 122:11076–11091, 2017.
- 385 Patrick T Gannon. *Influence of earth surface and cloud properties on the south Florida sea breeze*, volume 55. Department of  
386 Commerce, National Oceanic and Atmospheric Administration~, 1978.
- 387 Elizabeth S Garcia, Abigail L S Swann, Juan C Villegas, David D Breshears, Darin J Law, Scott R Saleska, and Scott C Stark.  
388 Synergistic ecoclimate teleconnections from forest loss in different regions structure global ecological responses. *PLoS ONE*,  
389 11(11):1–12, 2016. ISSN 19326203. doi: 10.1371/journal.pone.0165042.
- 390 Timothy J Garrett and Peter V. Hobbs. Long-Range Transport of Continental Aerosols over teh Atlantic Ocean and Their  
391 Effects on Cloud Structures. *Journal of the Atmospheric Sciences*, 52(16):2977–2984, 1995.
- 392 Sarah T. Gille, Stefan G. Llewellyn Smith, and Nicholas M. Statom. Global observations of the land breeze. *Geophysical  
393 Research Letters*, 32(5):1–4, 2005. ISSN 00948276. doi: 10.1029/2004GL022139.
- 394 Watson W. Gregg, Nancy W. Casey, and Charles R. McClain. Recent trends in global ocean chlorophyll. *Geophysical Research  
395 Letters*, 32(3):1–5, 2005. ISSN 00948276. doi: 10.1029/2004GL021808.
- 396 Charles R Harris, K Jarrod Millman, Stefan J van der Walt, Ralf Gommers, Pauli Virtanen, David Cournapeau, Eric Wieser,  
397 Julian Taylor, Sebastian Berg, Nathaniel J Smith, Robert Kern, Matti Picus, Stephan Hoyer, Marten H van Kerkwijk, Matthew  
398 Brett, Allan Haldane, Jaime Fernandez del Rio, Mark Wiebe, Pearu Peterson, Pierre Gerard-Marchant, Kevin Sheppard, Tyler  
399 Reddy, Warren Weckesser, Hameer Abbasi, Christoph Gohlke, and Travis E Oliphant. Array programming with NumPy.  
400 *Nature*, 585(7825):357–362, September 2020. doi: 10.1038/s41586-020-2649-2. Publisher: Springer Science and Business  
401 Media {LLC}.
- 402 Dennis L Hartmann. *Global physical climatology*, volume 103. Newnes, 2015.
- 403 Isaac M. Held and Brian J. Soden. WATER VAPOR FEEDBACK AND GLOBAL WARMING. *Annual Reviews of Energy and  
404 the Environment*, 25:441–4754, 2000. doi: <https://doi.org/10.1146/annurev.energy.25.1.441>. ISBN: 9781606929933.
- 405 Isaac M. Held, Mingfang Ting, and Hailan Wang. Northern winter stationary waves: Theory and modeling. *Journal of Climate*,  
406 15(16):2125–2144, 2002. ISSN 08948755. doi: 10.1175/1520-0442(2002)015<2125:NWSWTA>2.0.CO;2.

- 407 Hans Hersbach, Bill Bell, Paul Berrisford, Shoji Hirahara, András Horányi, Joaquín Muñoz-Sabater, Julien Nicolas, Carole  
408 Peubey, Raluca Radu, Dinand Schepers, Adrian Simmons, Cornel Soci, Saleh Abdalla, Xavier Abellan, Gianpaolo Balsamo,  
409 Peter Bechtold, Gionata Biavati, Jean Bidlot, Massimo Bonavita, Giovanna De Chiara, Per Dahlgren, Dick Dee, Michail  
410 Diamantakis, Rossana Dragani, Johannes Flemming, Richard Forbes, Manuel Fuentes, Alan Geer, Leo Haimberger, Sean  
411 Healy, Robin J. Hogan, Elías Hólm, Marta Janisková, Sarah Keeley, Patrick Laloyaux, Philippe Lopez, Cristina Lupu, Gabor  
412 Radnóti, Patricia de Rosnay, Iryna Rozum, Freja Vamborg, Sébastien Villaume, and Jean Noël Thépaut. The ERA5 global  
413 reanalysis. *Quarterly Journal of the Royal Meteorological Society*, 146(730):1999–2049, 2020. ISSN 1477870X. doi:  
414 10.1002/qj.3803.
- 415 S Hoyer and J Hamman. xarray: N-D labeled arrays and datasets in Python. *Journal of Open Research Software*, 5(1), 2017.  
416 doi: 10.5334/jors.148. Publisher: Ubiquity Press.
- 417 IPCC. Contribution of working group I to the Fourth Assessment Report of the Intergovernmental Panel on Climate Change:  
418 Summary for Policymakers. Technical report, 2007.
- 419 Ipcc. *Global Warming of 1.5°C: IPCC Special Report on impacts of global warming of 1.5°C above pre-industrial levels in  
420 context of strengthening response to climate change, sustainable development, and efforts to eradicate poverty*. Cambridge  
421 University Press, 1 edition, June 2022. ISBN 978-1-00-915794-0 978-1-00-915795-7. doi: 10.1017/9781009157940. URL  
422 <https://www.cambridge.org/core/product/identifier/9781009157940/type/book>.
- 423 Chris D. Jones, Vivek Arora, Pierre Friedlingstein, Laurent Bopp, Victor Brovkin, John Dunne, Heather Graven, Forrest  
424 Hoffman, Tatiana Ilyina, Jasmin G. John, Martin Jung, Michio Kawamiya, Charlie Koven, Julia Pongratz, Thomas Raddatz,  
425 James T. Randerson, and Sönke Zaehle. C4MIP-The Coupled Climate-Carbon Cycle Model Intercomparison Project:  
426 Experimental protocol for CMIP6. *Geoscientific Model Development*, 9(8):2853–2880, 2016. ISSN 19919603. doi:  
427 10.5194/gmd-9-2853-2016.
- 428 Axel Kleidon, Klaus Fraedrich, and Martin Heimann. A green planet versus a desert world: Estimating the maximum effect  
429 of vegetation on the land surface climate. *Climatic Change*, 44(4):471–493, 2000. ISSN 01650009. doi: 10.1023/A:  
430 1005559518889. Publisher: Springer ISBN: 0165-0009.
- 431 Gabriel J. Kooperman, Yang Chen, Forrest M. Hoffman, Charles D. Koven, Keith Lindsay, Michael S. Pritchard, Abigail L.S.  
432 Swann, and James T. Randerson. Forest response to rising CO<sub>2</sub> drives zonally asymmetric rainfall change over tropical  
433 continents. *Nature Climate Change*, 8(5):1–36, 2017. ISSN 17586798. doi: 10.1038/s41558-018-0144-7. URL <http://dx.doi.org/10.1038/s41558-018-0144-7>. Publisher: Springer US.
- 435 Randal D. Koster, Zhichang Guo, Paul A. Dirmeyer, Gordon Bonan, Edmond Chan, Peter Cox, Harvey Davies, C. T. Gordon,  
436 Shinjiro Kanae, Eva Kowalczyk, David Lawrence, Ping Liu, Cheng Hsuan Lu, Sergey Malyshev, Bryant McAvaney, Ken  
437 Mitchell, David Mocko, Taikan Oki, Keith W. Oleson, Andrew Pitman, Y. C. Sud, Christopher M. Taylor, Diana Verseghy,

- 438 Ratko Vasic, Yongkang Xue, and Tomohito Yamada. GLACE: The Global Land-Atmosphere Coupling Experiment. Part I:  
439 Overview. *Journal of Hydrometeorology*, 7(4):590–610, 2006. ISSN 1525755X. doi: 10.1175/JHM510.1.
- 440 Bernd Kärcher. Cirrus Clouds and Their Response to Anthropogenic Activities. *Current Climate Change Reports*, 3(1):45–57,  
441 2017. ISSN 21986061. doi: 10.1007/s40641-017-0060-3. Publisher: Current Climate Change Reports.
- 442 Marysa M Laguë. Progressive Mid-latitude Afforestation: Local and Remote Climate Impacts in the Framework of Two  
443 Coupled Earth System Models. Master's thesis, University of Washington, Seattle, WA, USA, 2016.
- 444 Marysa M. Laguë and Abigail L.S. Swann. Progressive midlatitude afforestation: Impacts on clouds, global energy transport,  
445 and precipitation. *Journal of Climate*, 29(15):5561–5573, 2016. ISSN 08948755. doi: 10.1175/jcli-d-15-0748.1.
- 446 Marysa M. Laguë, Gordon B. Bonan, and Abigail L. S. Swann. Separating the Impact of Individual Land Surface Properties on  
447 the Terrestrial Surface Energy Budget in both the Coupled and Uncoupled Land–Atmosphere System. *Journal of Climate*,  
448 32(18):5725–5744, 2019. ISSN 0894-8755. doi: 10.1175/jcli-d-18-0812.1.
- 449 Marysa M. Laguë, Abigail L. S. Swann, and William R. Boos. Radiative feedbacks on land surface change and associated  
450 tropical precipitation shifts. *Journal of Climate*, (2012):1–63, 2021. ISSN 0894-8755. doi: 10.1175/jcli-d-20-0883.1.
- 451 Chengfeng Li and Michio Yanai. The Onset and Interannual Variability of the Asian Summer Monsoon in Relation to Land-  
452 Sea Thermal Contrast. *Journal of Climate*, 9:358–375, 1996. doi: [https://doi.org/10.1175/1520-0442\(1996\)009<0358:TOAIVO>2.0.CO;2](https://doi.org/10.1175/1520-0442(1996)009<0358:TOAIVO>2.0.CO;2).
- 454 U. Lohmann. Aerosol effects on clouds and climate. *Space Science Reviews*, 125(1-4):129–137, 2006. ISSN 00386308. doi:  
455 10.1007/s11214-006-9051-8.
- 456 Elizabeth A. Maroon, Dargan M.W. Frierson, and David S. Battisti. The tropical precipitation response to Andes topography  
457 and ocean heat fluxes in an aquaplanet model. *Journal of Climate*, 28(1):381–398, 2015. ISSN 08948755. doi: 10.1175/  
458 JCLI-D-14-00188.1.
- 459 B. E. Medlyn, C. V. M. Barton, M. S. J. Broadmeadow, R. Ceulemans, P. De Angelis, M. Forstreuter, M. Freeman, S. B.  
460 Jackson, S. Kellomäki, E. Laitat, A. Rey, P. Roberntz, B. D. Sigurdsson, J. Strassemeyer, K. Wang, P. S. Curtis, and P. G.  
461 Jarvis. Stomatal conductance of forest species after long-term exposure to elevated CO<sub>2</sub> concentration: a synthesis. *New  
462 Phytologist*, 149(2):247–264, February 2001. ISSN 0028-646X, 1469-8137. doi: 10.1046/j.1469-8137.2001.00028.x. URL  
463 <https://onlinelibrary.wiley.com/doi/10.1046/j.1469-8137.2001.00028.x>.
- 464 Belinda E. Medlyn, REMKO A. Duursma, DEREK Eamus, David S. Ellsworth, I. Colin Prentice, CRAIG V.M. M Barton,  
465 Kristine Y. Crous, PAOLO De Angelis, Michael Freeman, and Lisa Wingate. Reconciling the optimal and empirical  
466 approaches to modelling stomatal conductance. *Global Change Biology*, 17(6):2134–2144, 2011. ISSN 13541013.

- 467 doi: 10.1111/j.1365-2486.2010.02375.x. URL <http://dx.doi.org/10.1111/j.1365-2486.2010.02375.x>.
- 468 Publisher: Blackwell Publishing Ltd ISBN: 1354-1013.
- 469 James I. L. Morison. Increasing atmospheric CO<sub>2</sub> and stomata. *New Phytologist*, 149(2):154–156, February 2001. ISSN  
470 0028-646X, 1469-8137. doi: 10.1046/j.1469-8137.2001.00042.x. URL <https://onlinelibrary.wiley.com/doi/10.1046/j.1469-8137.2001.00042.x>.
- 472 Ranga B Myneni, Sietse O. Los, and Compton J. Tucker. Satellite-based identification of linked vegetation index and sea  
473 surface temperature anomaly areas from 1982-1990 for Africa, Australia and South America. *Geophysical Research Letters*,  
474 23(7):729–732, 1996. doi: <https://doi.org/10.1029/96GL00266>.
- 475 E. D. Nilsson, J. Paatero, and M. Boy. Effects of air masses and synoptic weather on aerosol formation in the continental  
476 boundary layer. *Tellus B*, 53(4):462–478, September 2001. ISSN 0280-6509, 1600-0889. doi: 10.1034/j.1600-0889.2001.  
477 530410.x. URL <http://www.tellusb.net/index.php/tellusb/article/view/16619>.
- 478 G. R. North, J. G. Mengel, and D. A. Short. Simple energy balance model resolving the seasons and the continents: Application  
479 to the astronomical theory of the ice ages. *Journal of Geophysical Research*, 88(C11):6576–6586, 1983. ISSN 01480227.  
480 doi: 10.1029/JC088iC11p06576.
- 481 P. A. O’Gorman and C. J. Muller. How closely do changes in surface and column water vapor follow Clausius-Clapeyron  
482 scaling in climate change simulations? *Environmental Research Letters*, 5(2), 2010. ISSN 17489326. doi: 10.1088/  
483 1748-9326/5/2/025207.
- 484 D D Parrish and C J Hahn. INDICATIONS OF PHOTOCHEMICAL HISTORIES OF PACIFIC AIR MASSES FROM  
485 MEASUREMENTS trap held The method has been completely described Two UV-absorption coast , approximately 180 km  
486 northwest of San 123°44' W , elevation 20 m ). It Point Arena which protrudes. 97, 1992.
- 487 Sarah J. Perry, Shayne McGregor, Alex Sen Gupta, and Matthew H. England. Future Changes to El Niño–Southern Oscillation  
488 Temperature and Precipitation Teleconnections. *Geophysical Research Letters*, 44(20):10,608–10,616, 2017. ISSN 19448007.  
489 doi: 10.1002/2017GL074509.
- 490 Felix Pithan, Gunilla Svensson, Rodrigo Caballero, Dmitry Chechin, Timothy W. Cronin, Annica M. L. Ekman, Roel Neggers,  
491 Matthew D. Shupe, Amy Solomon, Michael Tjernström, and Manfred Wendisch. Role of air-mass transformations in exchange  
492 between the Arctic and mid-latitudes. *Nature Geoscience*, 11(11):805–812, November 2018. ISSN 1752-0894, 1752-0908.  
493 doi: 10.1038/s41561-018-0234-1. URL <http://www.nature.com/articles/s41561-018-0234-1>.
- 494 Franklin R. Robertson, Michael G. Bosilovich, and Jason B. Roberts. Reconciling land-ocean moisture transport variability in  
495 reanalyses with P - ET in observationally driven land surface models. *Journal of Climate*, 29(23):8625–8646, 2016. ISSN  
496 08948755. doi: 10.1175/JCLI-D-16-0379.1.

- 497 P J Sellers, L Bounoua, G J Collatz, D a. Randall, D a. Dazlich, S O Los, J a. Berry, I Fung, C J Tucker, C B Field, Others, T G  
498 Jensen, and Others. Comparison of radiative and physiological effects of doubled atmospheric CO<sub>2</sub> on climate. *SCIENCE-*  
499 *NEW YORK THEN WASHINGTON-*, 271(5254):1402–1405, 1996. ISSN 0036-8075. doi: 10.1126/science.271.5254.1402.  
500 Publisher: American Association for the Advancement of Science ISBN: 0036-8075.
- 501 Tiffany A. Shaw and Aiko Voigt. Land dominates the regional response to CO<sub>2</sub> direct radiative forcing. *Geophysical*  
502 *Research Letters*, 43(21), November 2016. ISSN 0094-8276, 1944-8007. doi: 10.1002/2016GL071368. URL <https://doi.org/10.1002/2016GL071368>.
- 503
- 504 S. C. Sherwood, R. Roca, T. M. Weckwerth, and N. G. Andronova. Tropospheric water vapor, convection, and climate. *Reviews*  
505 *of Geophysics*, 48(2):1–29, 2010. ISSN 87551209. doi: 10.1029/2009RG000301.
- 506 Brian J. Soden and Isaac M. Held. An Assessment of Climate Feedbacks in Coupled Ocean–Atmosphere Models. *Journal*  
507 *of Climate*, 19(14):3354–3360, 2006. ISSN 0894-8755. doi: 10.1175/JCLI3799.1. URL <http://dx.doi.org/10.1175/JCLI3799.1>. Publisher: American Meteorological Society ISBN: 0894-8755.
- 508
- 509 CJ Sonu, SP Murray, SA Hsu, JN Suhayda, and E Waddell. Sea Breeze and Coastal Processes. *Eos, Transactions American*  
510 *Geophysical Union*, 54(9):820–833, 1973.
- 511 Graeme L. Stephens. Cloud feedbacks in the climate system: A critical review. *Journal of Climate*, 18(2):237–273, 2005. ISSN  
512 08948755. doi: 10.1175/JCLI-3243.1.
- 513 Rowan T. Sutton, Buwen Dong, and Jonathan M. Gregory. Land/sea warming ratio in response to climate change: IPCC AR4  
514 model results and comparison with observations. *Geophysical Research Letters*, 34(2):2–6, 2007. ISSN 00948276. doi:  
515 10.1029/2006GL028164.
- 516 Abigail L S Swann, Forrest M Hoffman, Charles D Koven, and James T Randerson. Plant responses to increasing CO<sub>2</sub>  
517 reduce estimates of climate impacts on drought severity. *PNAS*, 113(36):10019–10024, 2016. ISSN 0027-8424. doi:  
518 10.1073/pnas.1604581113. arXiv: 1408.1149 ISBN: 1215421109.
- 519 Abigail L.S. S Swann, Inez Y. Fung, and John C.H. H Chiang. Mid-latitude afforestation shifts general circulation and tropical  
520 precipitation. *Proceedings of the National Academy of Sciences*, 109(3):712–716, January 2012. ISSN 0027-8424. doi:  
521 10.1073/pnas.1116706108. ISBN: 0027-8424.
- 522 R. H. White, D. S. Battisti, and G. H. Roe. Mongolian mountains matter most: Impacts of the latitude and height of asian  
523 orography on pacific wintertime atmospheric circulation. *Journal of Climate*, 30(11):4065–4082, 2017. ISSN 08948755.  
524 doi: 10.1175/JCLI-D-16-0401.1.
- 525 Robert Wood. Stratocumulus clouds. *Monthly Weather Review*, 140(8):2373–2423, 2012. ISSN 00270644. doi: 10.1175/  
526 MWR-D-11-00121.1.

		Wake Area (Low CO <sub>2</sub> )		Wake Area (High CO <sub>2</sub> )		Δ Wake Area (High-Low CO <sub>2</sub> )	
		DJF	JJA	DJF	JJA	DJF	JJA
bgcCO <sub>2</sub>	Multi-model Mean	5.39 ×10 <sup>6</sup> km <sup>2</sup>	3.80 ×10 <sup>6</sup> km <sup>2</sup>	5.38 ×10 <sup>6</sup> km <sup>2</sup>	4.00 ×10 <sup>6</sup> km <sup>2</sup>	-7.27 ×10 <sup>3</sup> km <sup>2</sup>	1.61 ×10 <sup>5</sup> km <sup>2</sup>
radCO <sub>2</sub>	Multi-model Mean	5.47 ×10 <sup>6</sup> km <sup>2</sup>	3.82 ×10 <sup>6</sup> km <sup>2</sup>	4.88 ×10 <sup>6</sup> km <sup>2</sup>	3.77 ×10 <sup>6</sup> km <sup>2</sup>	-5.84 ×10 <sup>5</sup> km <sup>2</sup>	-4.99 ×10 <sup>4</sup> km <sup>2</sup>
fullCO <sub>2</sub>	Multi-model Mean	5.48 ×10 <sup>6</sup> km <sup>2</sup>	3.80 ×10 <sup>6</sup> km <sup>2</sup>	5.05 ×10 <sup>6</sup> km <sup>2</sup>	3.88 ×10 <sup>6</sup> km <sup>2</sup>	-4.31 ×10 <sup>5</sup> km <sup>2</sup>	7.42 ×10 <sup>5</sup> km <sup>2</sup>
ERA5 1979-2019	Mean	6.16 ×10 <sup>6</sup> km <sup>2</sup>	4.25 ×10 <sup>6</sup> km <sup>2</sup>				

**Table S1.** Absolute wake area and change in wake area between years 1-20 (Low CO<sub>2</sub>) and years 121-140 (High CO<sub>2</sub>) of the 1pctCO<sub>2</sub>-bgc, 1pctCO<sub>2</sub>-rad, and 1pctCO<sub>2</sub>-full simulations. Wake areas for the 1979-2019 ERA5 mean are also shown.

- 527 Guoxiong Wu, Yimin Liu, Bian He, Qing Bao, Anmin Duan, and Fei Fei Jin. Thermal controls on the asian summer monsoon.  
 528 *Scientific Reports*, 2:1–7, 2012. ISSN 20452322. doi: 10.1038/srep00404.
- 529 Xiaosong Yang and Timothy Delsole. Systematic comparison of enso teleconnection patterns between models and observations.  
 530 *Journal of Climate*, 25(2):425–446, 2012. ISSN 08948755. doi: 10.1175/JCLI-D-11-00175.1.
- 531 Claire M. Zariskas, Abigail L. Swann, Marysa M. Laguë, Kyle C. Armour, and James T. Randerson. Plant Physiology Increases  
 532 the Magnitude and Spread of the Transient Climate Response to CO<sub>2</sub> in CMIP6 Earth System Models. *Journal of Climate*,  
 533 33(19):8561–8578, 2020a. ISSN 0894-8755. doi: 10.1175/jcli-d-20-0078.1.
- 534 Claire M. Zariskas, Abigail L. S. Swann, Marysa M. Laguë, Kyle C. Armour, and James T. Randerson. Plant Physiology  
 535 Increases the Magnitude and Spread of the Transient Climate Response to CO<sub>2</sub> in CMIP6 Earth System Models. *Journal*  
 536 *of Climate*, 33(19):8561–8578, October 2020b. ISSN 0894-8755, 1520-0442. doi: 10.1175/JCLI-D-20-0078.1. URL  
 537 <https://journals.ametsoc.org/doi/10.1175/JCLI-D-20-0078.1>.

## 538 Supplemental Figures & Tables

539

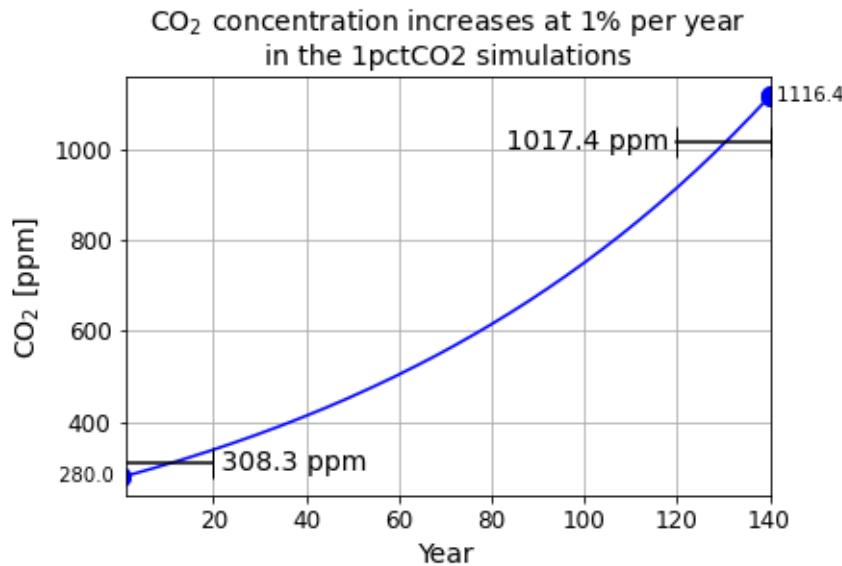


**Figure S1.** Time series showing the CO<sub>2</sub> concentration each year in the 1pcCO<sub>2</sub> simulations, with CO<sub>2</sub> increasing 1% per year for 140 years. CO<sub>2</sub> starts at 280 ppm (pre-industrial levels) and reaches 1116 ppm (roughly 4x pre-industrial levels) in year 140. The average CO<sub>2</sub> in the first 20 years (“low CO<sub>2</sub>”) is 308 ppm while the average CO<sub>2</sub> for years 121-140 (“high CO<sub>2</sub>”) is 1017 ppm.

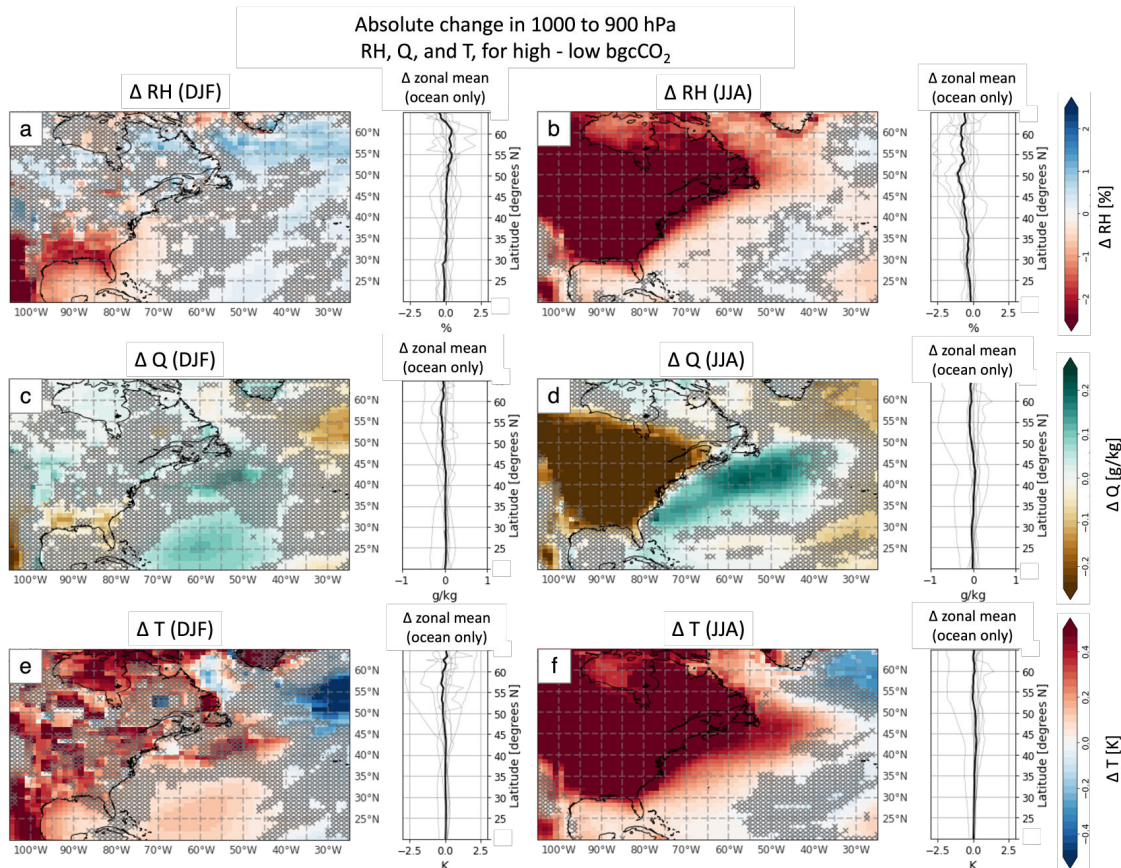


**Figure S2.** Change in the RH (top),  $q$  (middle), and  $T$  (bottom) fields (*not* the wake) in winter (left) and summer (right) for high-low bgcCO<sub>2</sub> in the C4MIP simulations. Hatching indicates where less than 6/9 models agree on sign. The zonal mean over the Atlantic Ocean is shown next to each map, with the multimodel mean in black and individual models in grey.

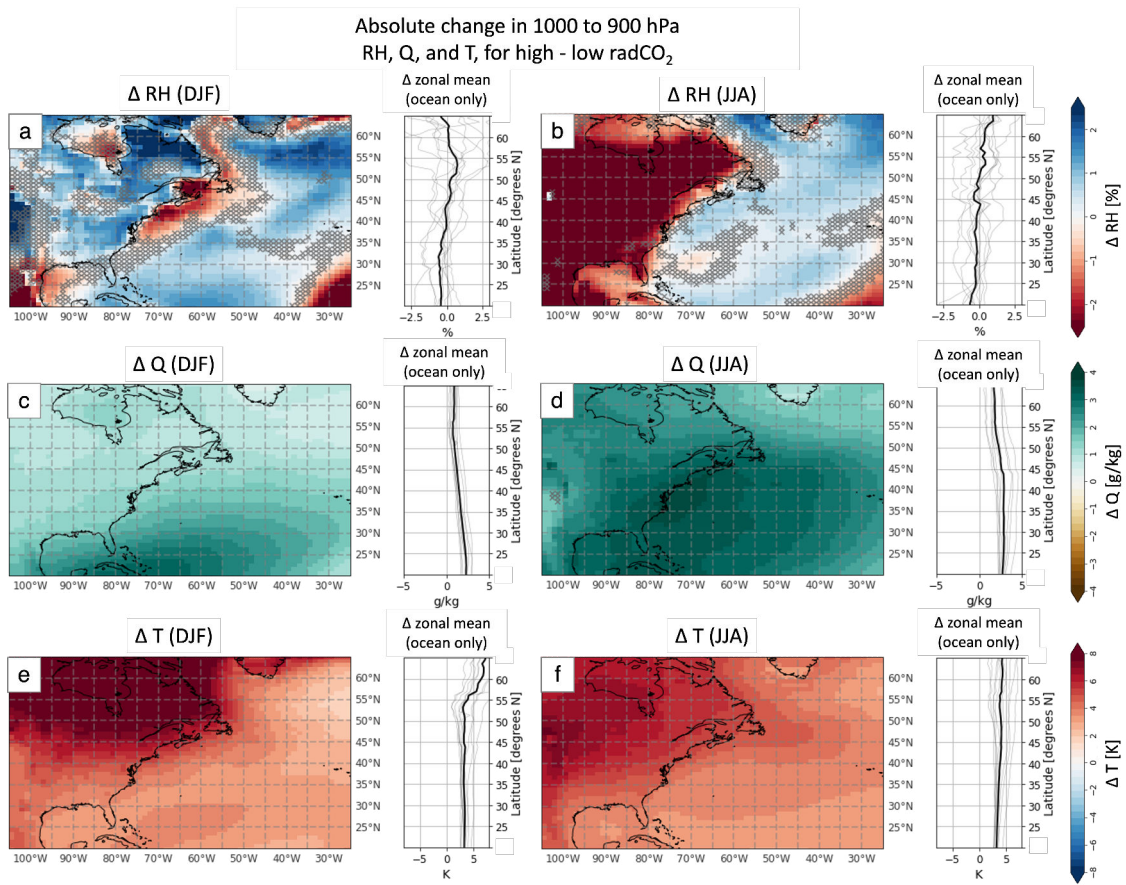


**Figure S3.** Change in the  $RH$  (top),  $q$  (middle), and  $T$  (bottom) fields (not the wake) in DJF (left) and JJA (right) for high-low  $\text{radCO}_2$  in the C4MIP simulations. Hatching indicates where less than 6/9 models agree on sign. The zonal mean over the Atlantic Ocean is shown next to each map, with the multimodel mean in black and individual models in grey.

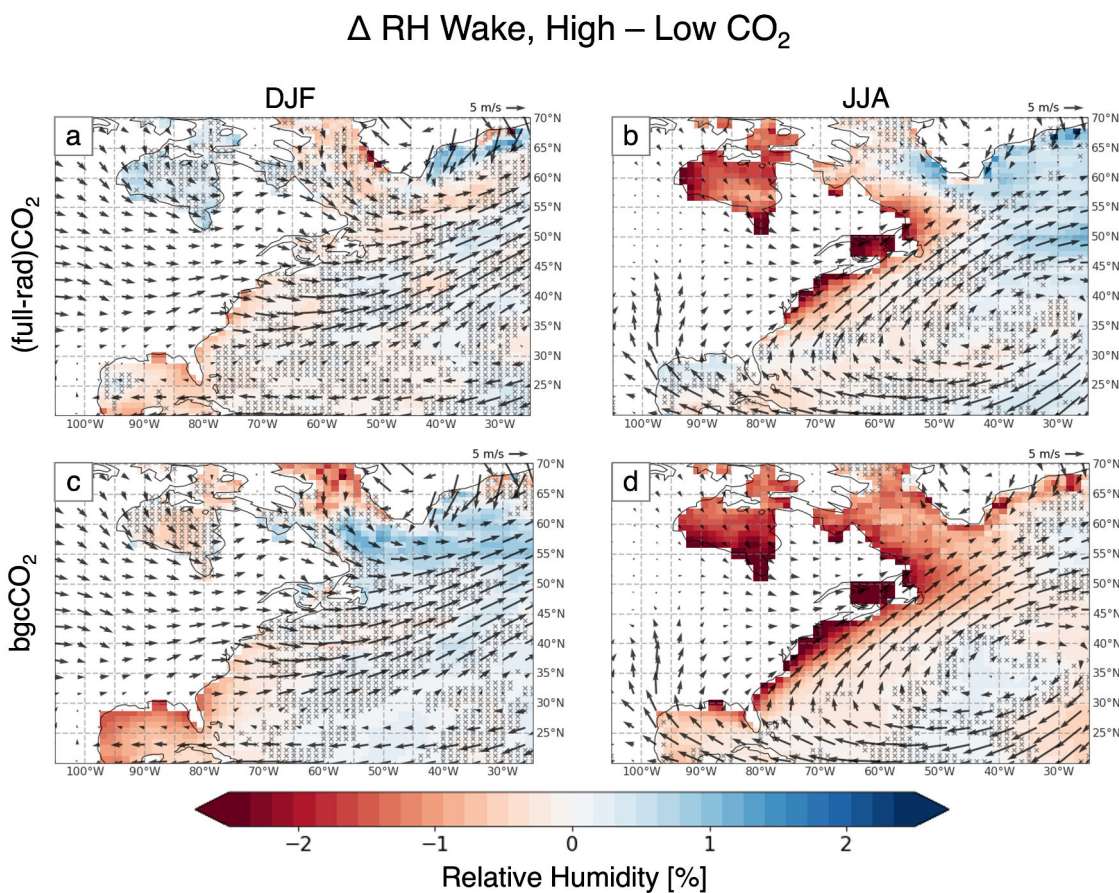


**Figure S4.** Change in the *RH* wake due to the bgc effects of CO<sub>2</sub> from the fullCO<sub>2</sub>-radCO<sub>2</sub> simulations (top), and the bgcCO<sub>2</sub> simulations (bottom) for winter (left) and summer (right). Hatching indicates where less than 6/9 models agree on sign.

$\Delta$  Specific Humidity Wake, High – Low CO<sub>2</sub>

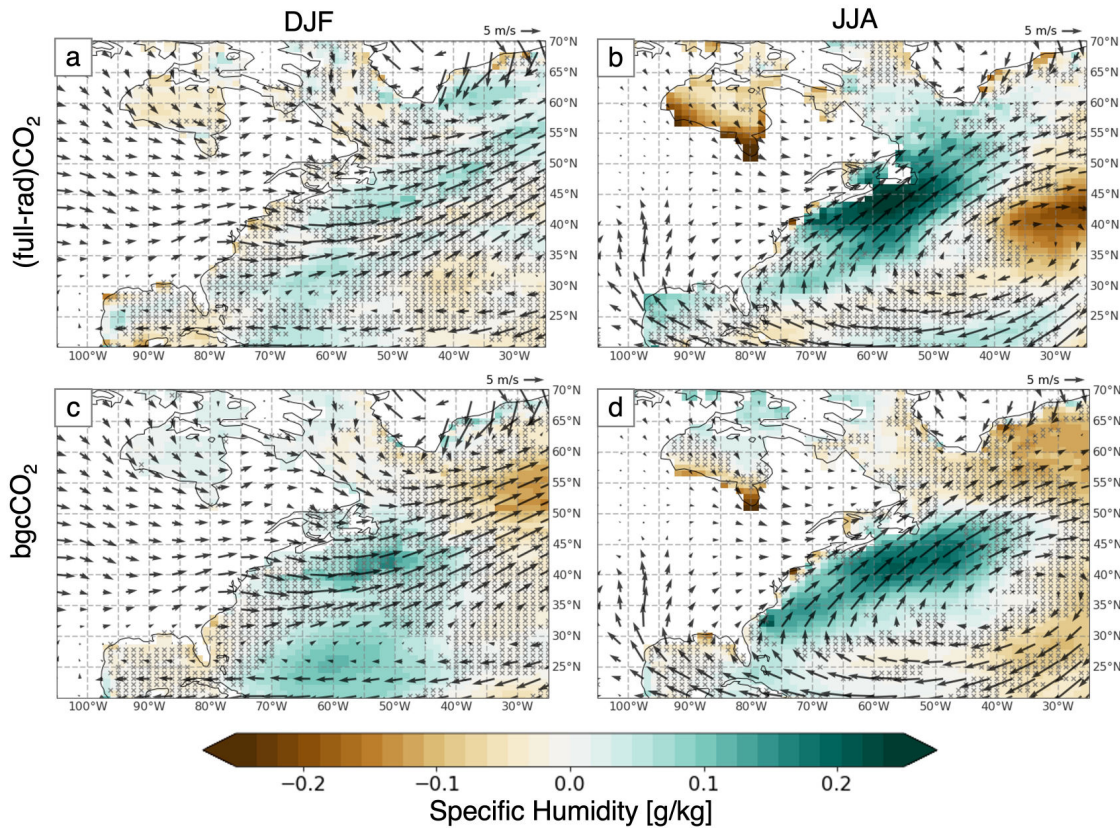


**Figure S5.** Change in the specific humidity wake due to the bgc effects of CO<sub>2</sub> from the fullCO<sub>2</sub>-radCO<sub>2</sub> simulations (top), and the bgcCO<sub>2</sub> simulations (bottom) for winter (left) and summer (right). Hatching indicates where less than 6/9 models agree on sign.

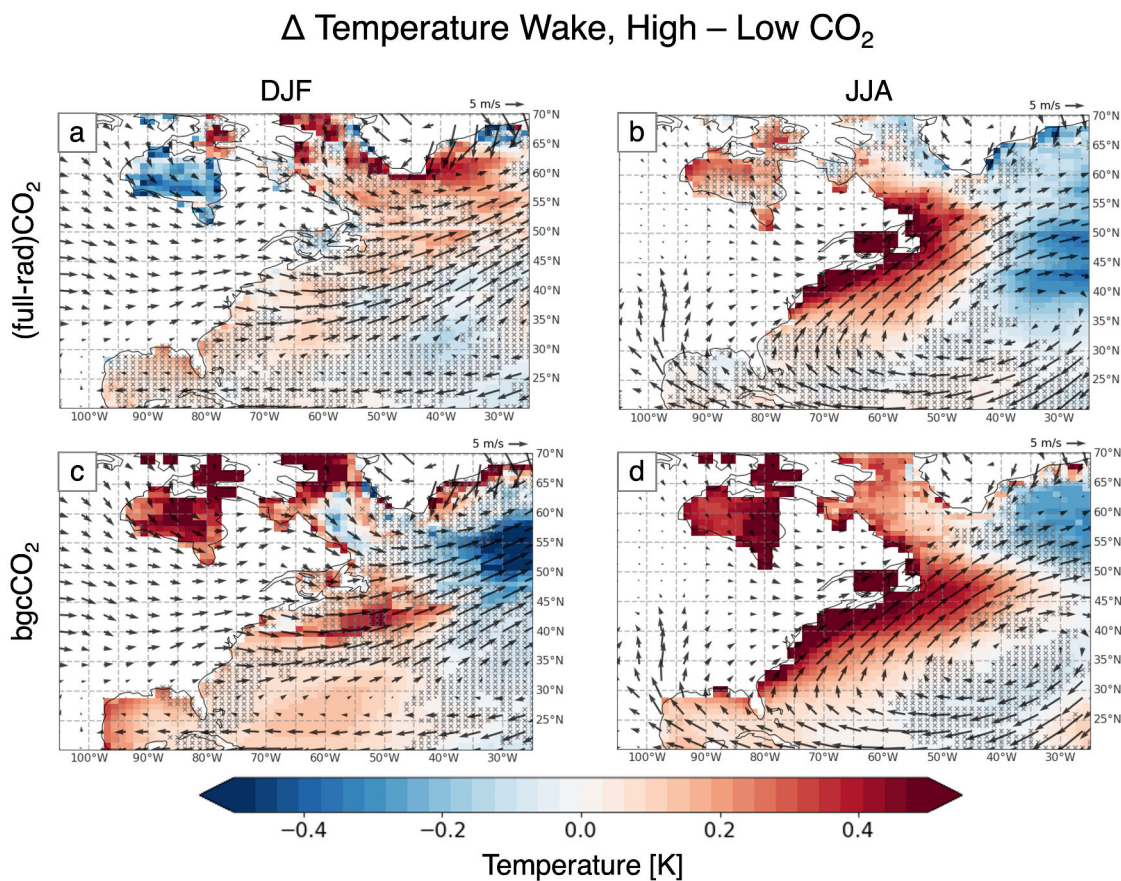


**Figure S6.** Change in the temperature wake due to the bgc effects of CO<sub>2</sub> from the fullCO<sub>2</sub>-radCO<sub>2</sub> simulations (top), and the bgcCO<sub>2</sub> simulations (bottom) for winter (left) and summer (right). Hatching indicates where less than 6/9 models agree on sign.

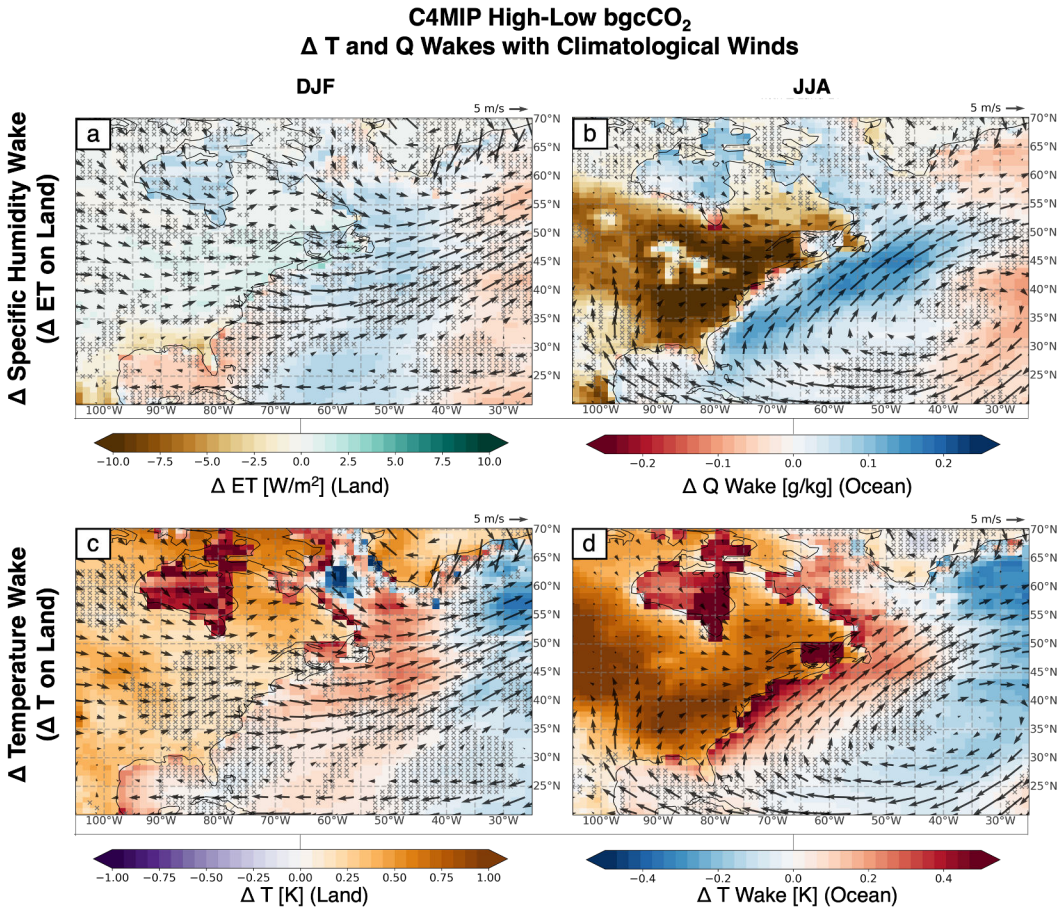


**Figure S7.** Change in the  $q$  (top) and  $T$  (bottom) wakes with increased bgcCO<sub>2</sub> are shown over the ocean, while changes in ET (top) and  $T$  (bottom) are shown over land. Winter changes are shown in the left column while summer changes are shown in the right column. Hatching indicates where less than 6/9 models agree on sign.

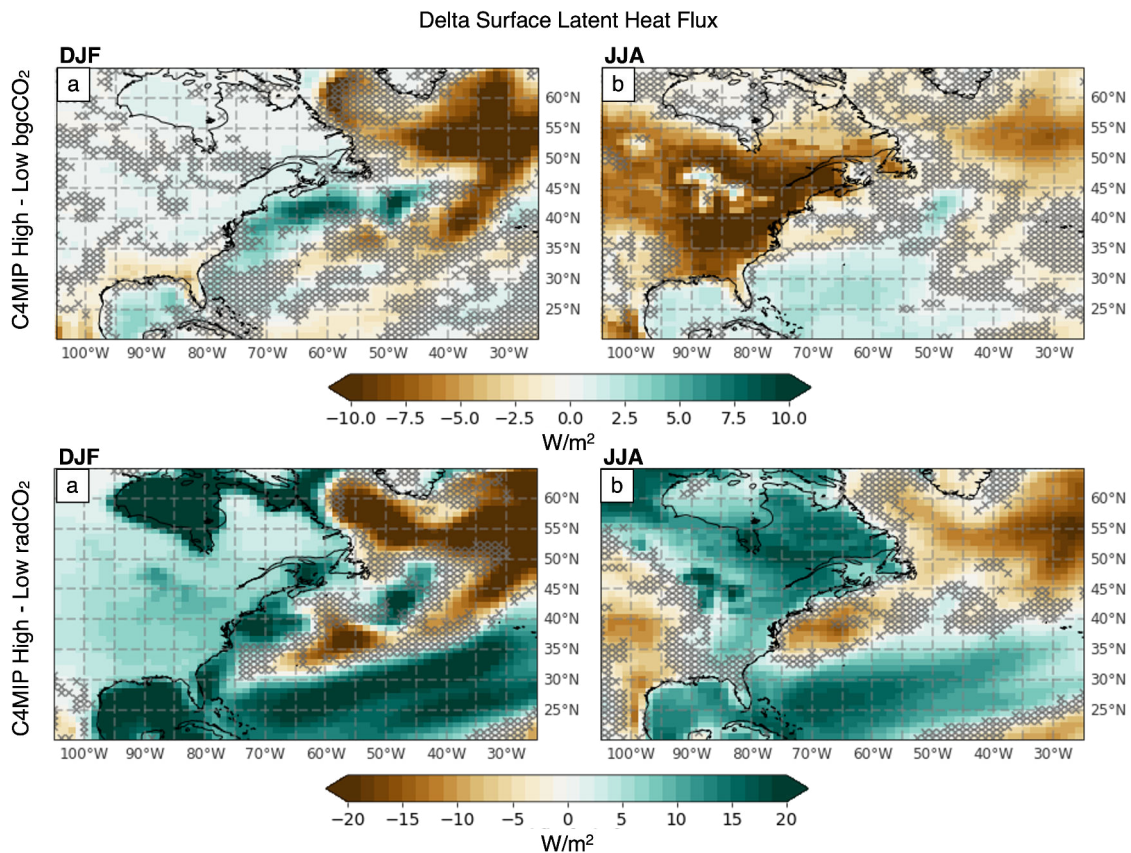


**Figure S8.** Change in surface latent heat flux in DJF (left) and JJA (right) for high-low bgcCO<sub>2</sub> (top) and radCO<sub>2</sub> (bottom) in the C4MIP simulations. Hatching indicates where less than 6/9 models agree on sign.

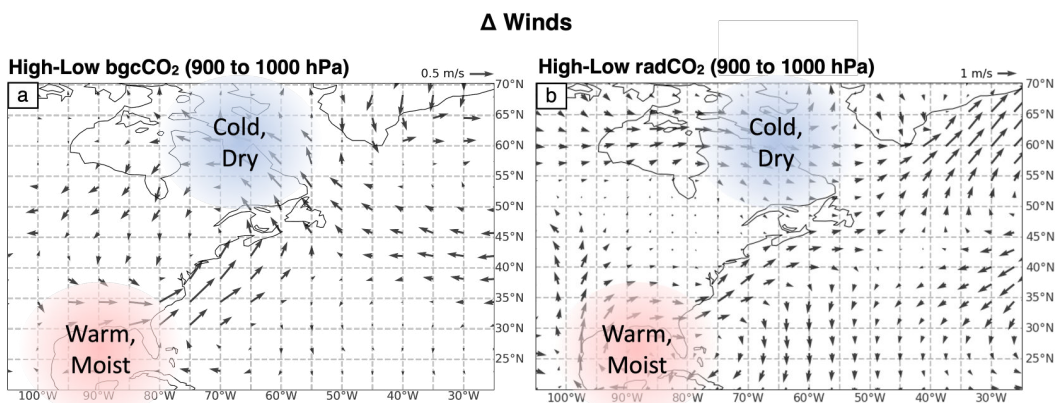


**Figure S9.** Change in winds for high-low bgcCO<sub>2</sub> (left) and radCO<sub>2</sub> (right) averaged from the surface to 900 hPa. The anomalous cyclonic circulation brings warm, high moisture content air from the south up along the east coast of the continent into regions with climatologically cooler, drier air.

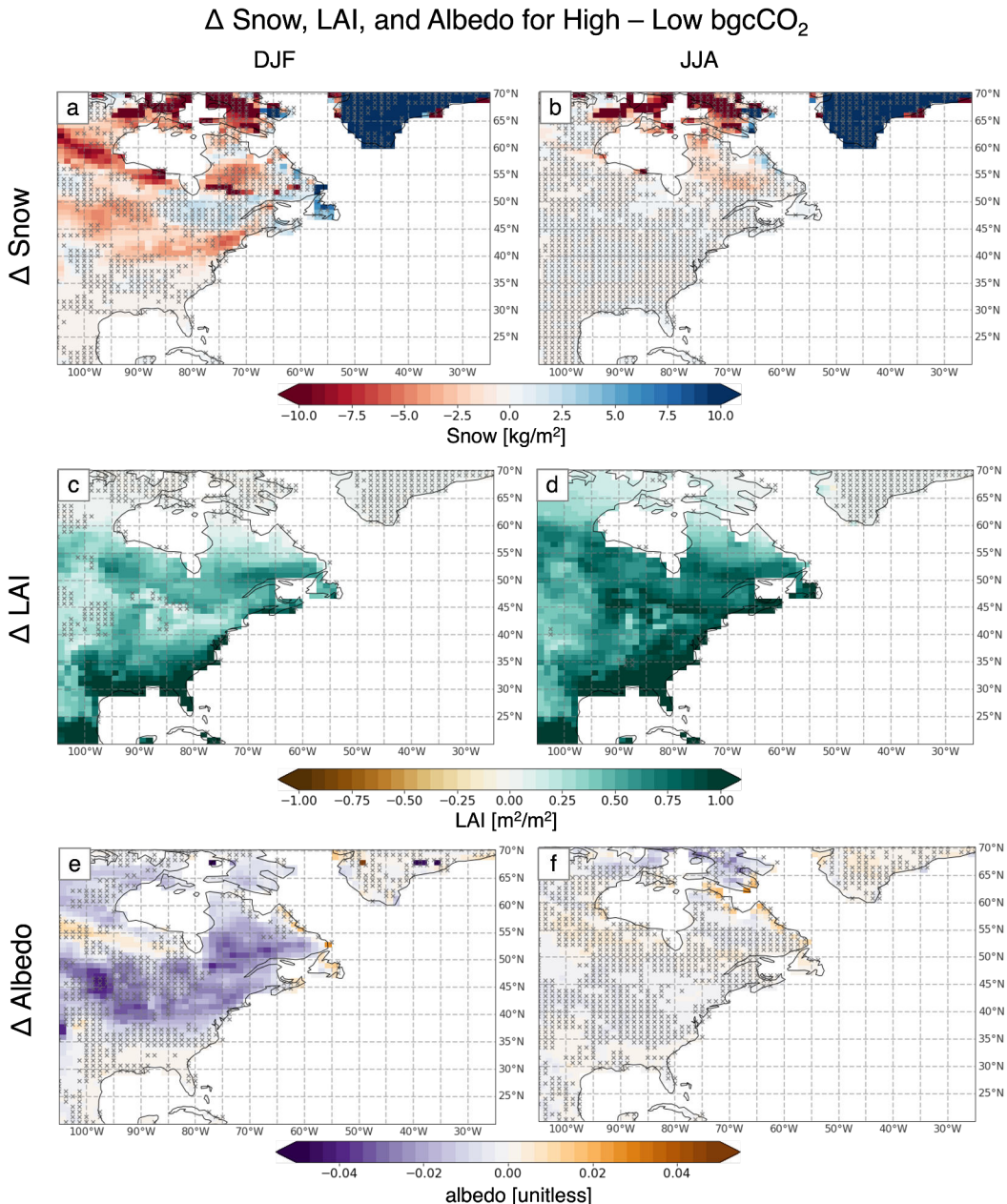


**Figure S10.** Change in snow cover (top), LAI (middle), and land albedo (bottom) in DJF (left) and JJA (right) for high-low bgCO<sub>2</sub> in the C4MIP simulations. Note that only 7 of the C4MIP models are used here (models where snow information was available: CNRM-ESM2-1, ACCESS-ESM1-5, IPSL-CM6A-LR, MIROC-ES2L, UKESM1-0-LL, MPI-ESM1-2-LR, CESM2). Hatching indicates where less than 5/7 models agree on sign.

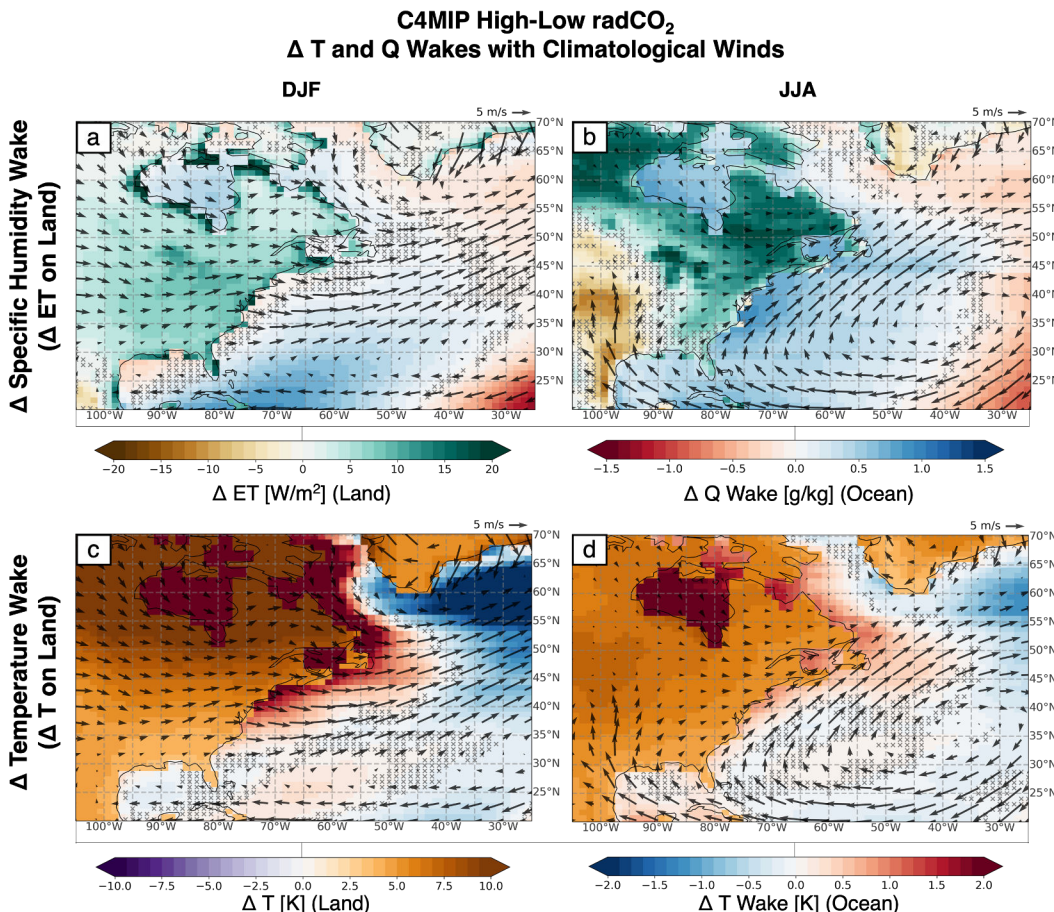


**Figure S11.** Change in the  $q$  (top) and  $T$  (bottom) wakes with increased  $\text{radCO}_2$  are shown over the ocean, while changes in  $ET$  (top) and  $T$  (bottom) are shown over land. Hatching indicates where less than 6/9 models agree on sign.

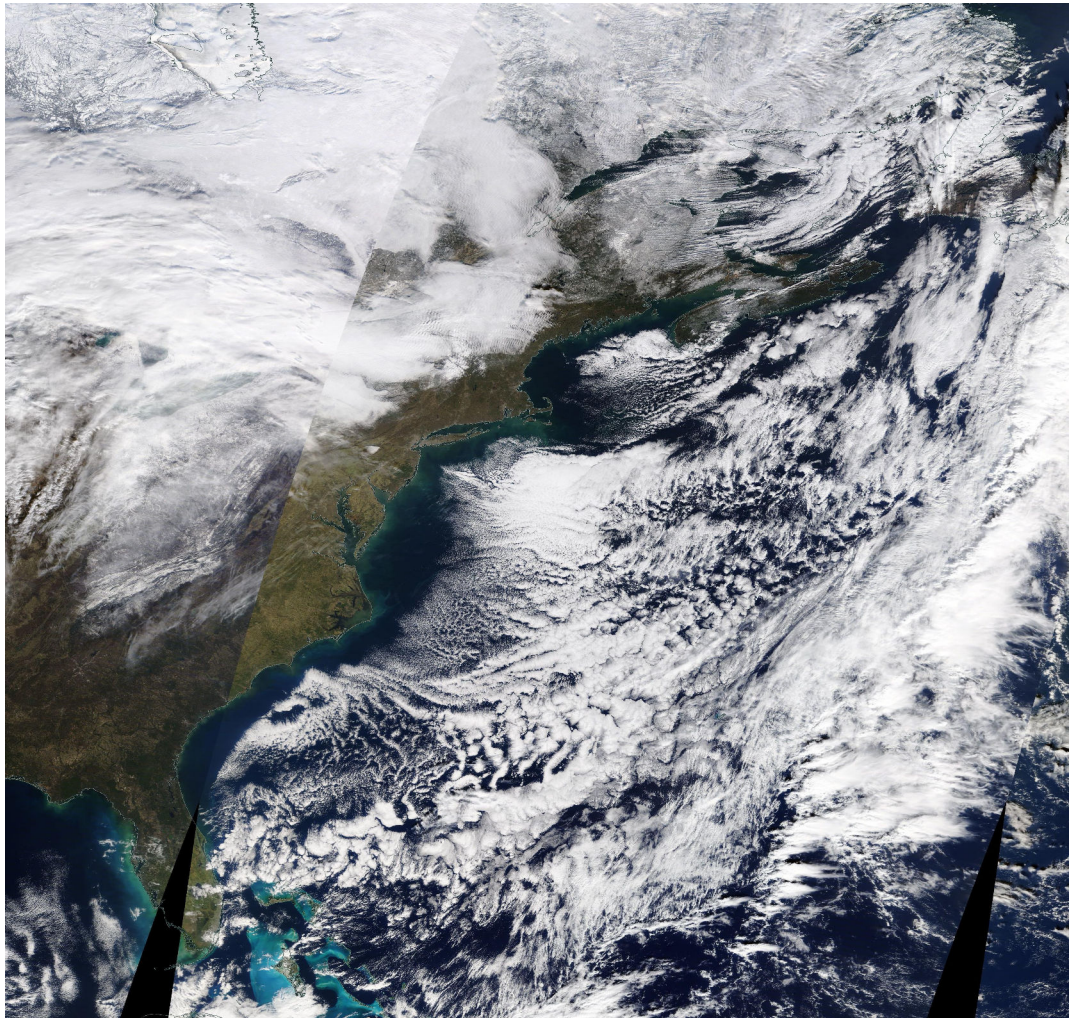


**Figure S12.** Terra/MODIS satellite image from NASA Worldview showing a cloud-free band of oceanic air downwind of the North American east coast. Date: Dec. 27, 2020. Source:

<https://worldview.earthdata.nasa.gov/?v=-110.17945652585333,17.05090683269548,-39.0207911550563,54.952779290613066&t=2020-12-27-T14%3A00%3A00Z>